Master Thesis DIPL-MSC-215

Investigation of Stress Analysis in Gear Simulations Using Different Model Order Reduction Techniques

from
Iosu Oloriz del Rosario

Advisor: Prof. Dr.–Ing. Prof. E.h. P. Eberhard
Dipl.-Ing. D. Schurr
Dipl.-Ing. P. Holzwarth

Universität Stuttgart
Institut für Technische und Numerische Mechanik
Prof. Dr.–Ing. Prof. E.h. P. Eberhard

June 2014

Contents

Chapter 1

Introduction

Computer aided simulations are increasingly being used in engineering. Simulation allows the designer to reduce the development time of a product as well as the number of prototypes. This makes it possible to work iteratively in an efficient manner with reduced costs and capacity, as change-implementation time decreases and less waste is produced.

Nowadays gear wheels are normally lightweight optimized parts (e.g. weight reduction in automotive gearboxes is essential to minimize the weight of the whole automobile) and should underlie high dynamic forces in order to ensure fast response of the system. Consequently, rigid body models of gears are not useful when precise simulations are needed. Elastic models are mandatory.

The elastic performance of gears can be simulated with different approaches: as a finite-element system or as an elastic multibody system. In this thesis, the latter is used. Using an elastic multibody system allows the researcher to reduce computational times compared to an equivalent finite-element simulation, while still achieving good quality results compared to the finite-element technique.

1.1 Objective

The main objective of this work is to simulate the contact between gears and determine if the stress values on the flank of the gear computed with the elastic multibody approach are similar to those obtained with the finite element approach. In order to do this, different model reduction techniques will be used. The reduction matrices will be computed using the *MatMorembs* software. Different reduction matrices will be assembled and tested in order to determine which is most suitable to solve this problem.

The time integration of the problem is done with the *GTM* software, i.e. Gear Train Module, [Ziegler12]. *GTM* solves both the interaction between the gears and integrates the equations of the elastic multibody system. In order to measure the quality of the results obtained with *GTM*, a finite-element model is made and solved in *Abaqus*. The results provided by *Abaqus* will be the benchmark with which all the results obtained in *GTM* are compared.

1.2 Structure of this thesis

In Chapter 2, the theoretical background of this thesis is presented. An introduction to elastic multibody mechanics and contact mechanics is undertaken and an overview of all the reduction techniques used in this work is presented.

In Chapter 3, a simpler model, made with a beam and a single force acting at one arbitrary node, is used as a first approach in order to discover which reduction techniques are most suitable and have more potential. Also, it facilitates the detection of errors and limitations that need to be taken into account later when working with the gears.

In Chapter 4, the gears used in this thesis are introduced. Simulation work is performed in two stages. In the first stage, one gear is loaded with a single force. Once the results are satisfactory the contact problem is set up with two different gears and the stresses are computed.

Finally, an overview of the results is presented in Chapter 5.

Chapter 2

Theoretical Background

In this chapter the main theoretical background for the thesis, which is necessary to understand this work, is presented. Firstly, in Section 2.1, the concept of multibody systems and the approach taken in this work to solve the problem is introduced. Later in Section 2.2, an overview of all the reduction techniques used in this thesis is carried out. In Section 2.3, a rough outline of the theory of contact mechanics is given. Finally, in Section 2.4, the stress recovery techniques are introduced.

2.1 Elastic Multibody System

In order to solve problems with gear interaction, a multibody system (MBS) approach is used in this thesis. It is possible to define a multibody system as a set of rigid solids interacting in different ways, for example, having contact.

In the case of this thesis, as the elastic deformation in the flanks of the gears is not negligible, a generalization of the MBS formulation is needed. In this generalization, the elastic deformation of the bodies has to be considered. This necessity gives rise to the elastic multibody system formulation, from here on referred to as EMBS. There are different ways of modeling an EMBS, primarily two as stated in [NowakowskiEtAl12]: the absolute nodal coordinate formulation and the floating frame of reference formulation.

Working with gear trains, elastic deformations are small in comparison with the rigid body motion, so the floating frame of reference formulation has been chosen and is used in this work. The idea behind this formulation is to model the absolute displacement of a body as a combination of a nonlinear rigid body motion of a reference frame attached to the body, and a linear elastic deformation with respect to the reference frame.

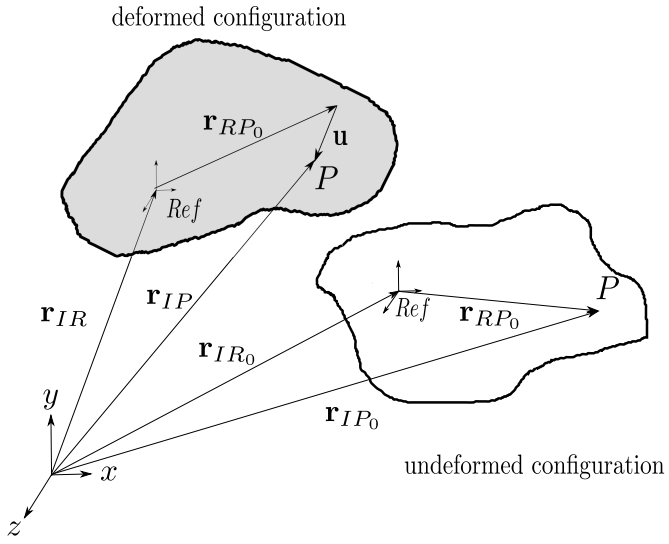

Figure 2.1: Floating frame of reference.

Therefore, if the movement of a solid is represented by the position variation of one arbitrary point P of the solid, the following formula holds true (see Fig. 2.1)

$$\boldsymbol{r}_{IP}(t) = \boldsymbol{r}_{IR}(t) + \boldsymbol{r}_{RP} + \boldsymbol{u}_p(t). \tag{2.1}$$

Displacement with time of point P is obtained by superposing the classical rigid motion displacement of P, $\boldsymbol{r}_{IR}(t) + \boldsymbol{r}_{RP}$ and a movement associated with only the linear elastic deformation of the body in the vicinity of P, $\boldsymbol{u}_p(t)$.

This elastic deformation is computed using the Ritz approach, see [NowakowskiEtAl12] and [MeirovitchKwak90],

$$\boldsymbol{u}_p(\boldsymbol{r}_{RP}, t) = \boldsymbol{\Phi}(\boldsymbol{r}_{RP}, t) \cdot \boldsymbol{q}_e(t), \tag{2.2}$$

where $\boldsymbol{q}_e$ represents the elastic coordinates of a finite element model and $\boldsymbol{\Phi}$ represents elastic shape functions [SchwertassekWallrappShabana99, Eberhard00].

The equation of motion of a general multibody system, [Shabana98], can be represented as

$$\boldsymbol{M}(\boldsymbol{q}) \cdot \ddot{\boldsymbol{q}} + \boldsymbol{k}(\dot{\boldsymbol{q}}, \boldsymbol{q}, t) = \boldsymbol{g}(\dot{\boldsymbol{q}}, \boldsymbol{q}, t), \tag{2.3}$$

in which $\boldsymbol{M}$ represents the mass matrix of the whole system, which is symmetrical and positive definte (the kinetic energy, if the system has a non-zero velocity is always greater than zero). Vector $\boldsymbol{q}$ is the set of generalized coordinates of the system; $\boldsymbol{k}$ (gyroscopic forces) and $\boldsymbol{g}$ (applied forces) are the forces acting on the system.

Focusing now on one body, the elastic movement can be characterized as

$$\boldsymbol{M}_e \cdot \ddot{\boldsymbol{q}}_e + \boldsymbol{K}_e \cdot \dot{\boldsymbol{q}}_e = \boldsymbol{f}_e, \tag{2.4}$$

in which $\boldsymbol{q}_e$ is the set of elastic coordinates and $\boldsymbol{M}_e$ and $\boldsymbol{K}_e$ are the elastic mass and stiffness matrices, respectively. It is also possible to consider dissipative effects introducing an elastic damping matrix in Eq. (2.4). Usually the Damping matrix is computed as a combination of both the mass and stiffness matrices and leads to

$$\boldsymbol{D}_e = \alpha \boldsymbol{M}_e + \beta \boldsymbol{K}_e \quad \text{where} \quad \alpha, \beta \ > 0. \tag{2.5}$$

In this work, the damping matrix, when considered, has been computed with $\alpha = 0$.

Combining the elastic and the rigid body motion Eq. (2.6) can describe the motion of one body as

$$\begin{bmatrix} \boldsymbol{M}_r & \boldsymbol{M}_{re} \\ \boldsymbol{M}_{er} & \boldsymbol{M}_e \end{bmatrix} \cdot \begin{bmatrix} \ddot{\boldsymbol{q}}_r \\ \ddot{\boldsymbol{q}}_e \end{bmatrix} = \begin{bmatrix} \boldsymbol{h}_r \\ \boldsymbol{h}_e \end{bmatrix}. \tag{2.6}$$

The matrix $\boldsymbol{M}_r$ is the mass matrix associated with the rigid body motion. Matrices $\boldsymbol{M}_{re}$, and $\boldsymbol{M}_{er}$ are the coupling matrices between the rigid body motion and the elastic deformations. Vector $\ddot{\boldsymbol{q}}_r$ refers to the translational and rotational accelerations in the case of a rigid body motion. Finally, vector $\boldsymbol{h}$ represents the forces acting on the body.

With the help of traditional rigid body equations, see [Agullo00], from a reference frame attached to the body at point O

$$\boldsymbol{F} = m\boldsymbol{a}_c \tag{2.7}$$

and

$$\boldsymbol{M}_O = \frac{\mathrm{d}\boldsymbol{H}_O}{\mathrm{d}t} + m(\boldsymbol{c} \times \boldsymbol{a}_O) \tag{2.8}$$

it is possible to further develop the Eq. (2.6). In Eq. (2.7) and Eq. (2.8) $\boldsymbol{a}_c$ is the acceleration of the center of gravity of the body in the inertial frame. $\boldsymbol{F}$, $\boldsymbol{M}$ are the external forces and torques applied to the body. Vector $\boldsymbol{c}$ is the position of the center of gravity, m is the mass of the body and $\boldsymbol{H}$ is the angular momentum of the body characterized in O.

Finally, Eq. (2.6) is transformed into the following shape, see [JalonBayo94]

$$\begin{bmatrix} m\boldsymbol{E} & m\tilde{\boldsymbol{c}} & \boldsymbol{C}_t^T \\ m\tilde{\boldsymbol{c}} & \boldsymbol{I} & \boldsymbol{C}_r^T \\ \boldsymbol{C}_t & \boldsymbol{C}_r & \boldsymbol{M}_e \end{bmatrix} \cdot \begin{bmatrix} \dot{\boldsymbol{v}} \\ \dot{\boldsymbol{\omega}} \\ \ddot{\boldsymbol{q}}_e \end{bmatrix} = \boldsymbol{h}. \tag{2.9}$$

In vector $\boldsymbol{h}$, all the forces and torques acting on the body are considered. Matrix $\boldsymbol{I}$ is the inertial tensor characterized at point O. Tensor $\tilde{\boldsymbol{c}}$ is the tensor associated with the position of the center of gravity (COG) of the body and $\boldsymbol{E}$ is the unitary matrix. $\boldsymbol{C}_t$ and $\boldsymbol{C}_r$ are matrices associated with the coupling of the rigid body motion and the elastic deformation. With this, integrating Eq. (2.9) is possible to obtain the solution to the problem.

2.2 Model order reduction

When modeling an elastic body with finite-element discretization, the immediate consequence is the huge number of nodal coordinates that appear. Therefore, in general, finite-element modeling is followed by a model order reduction process before integrating the system equations. The main idea behind model reduction is to eliminate some of the elastic coordinates of the system in a way that all the relevant information is approximated within the new reduced model:

$$\boldsymbol{q}_e \approx \boldsymbol{V} \cdot \boldsymbol{q}_{red}. \tag{2.10}$$

Matrix $\boldsymbol{V}$ is the reduction matrix and its columns span the sub-space in which the original set of coordinates is projected. Combining Eq. (2.10) and Eq. (2.4), supposing $\boldsymbol{V}$ to be time invariant, it is possible to obtain the elastic equation of the reduced model

$$\boldsymbol{V}^T \cdot \boldsymbol{M}_e \cdot \boldsymbol{V} \cdot \ddot{\boldsymbol{q}}_{red} + \boldsymbol{V}^T \cdot \boldsymbol{K}_e \cdot \boldsymbol{V} \cdot \boldsymbol{q}_{red} = \boldsymbol{V}^T \cdot \boldsymbol{f}_e, \tag{2.11}$$

$$\boldsymbol{M}_{red} \cdot \ddot{\boldsymbol{q}}_{red} + \boldsymbol{K}_{red} \cdot \boldsymbol{q}_{red} = \boldsymbol{f}_{red}. \tag{2.12}$$

2.2.1 Reduction by projection

If the set of original elastic coordinates is contained in $\mathbb{R}^N$, the idea is to project the vector $\boldsymbol{q}_e$ into a lower dimension subspace $\boldsymbol{\nu}$ contained in $\mathbb{R}^n$ in an effort to minimize the error between the original and the projected vector.

One matrix $\boldsymbol{P}$ is a projector (see [Griffer10]), if, and only if,

$$\boldsymbol{P} = \boldsymbol{P}^2 \tag{2.13}$$

holds true. If $\boldsymbol{P}$ is a projector then every vector $\boldsymbol{v} \in \mathbb{R}^N$ can be projected into $\boldsymbol{\nu}$ being premultiplied by $\boldsymbol{P}$. In the case of the elastic coordinates, it is possible to write

$$\hat{\boldsymbol{q}}_e = \boldsymbol{P} \cdot \boldsymbol{q}_e \tag{2.14}$$

and

$$\boldsymbol{q}_e = \boldsymbol{P} \cdot \boldsymbol{q}_e + (\boldsymbol{E} - \boldsymbol{P}) \cdot \boldsymbol{q}_e = \hat{\boldsymbol{q}}_e + \boldsymbol{\epsilon} \tag{2.15}$$

where $\boldsymbol{\epsilon}$ is the residual.

As the only condition for being a projector is Eq. (2.13) it is possible to define $\boldsymbol{P}$ in the following manner:

$$\boldsymbol{P} = \boldsymbol{X} \cdot \begin{bmatrix} \boldsymbol{E}_n & \boldsymbol{0} \\ \boldsymbol{0} & \boldsymbol{0}_{N-n} \end{bmatrix} \cdot \boldsymbol{X}^{-1}. \tag{2.16}$$

Matrix $\boldsymbol{X}$ can be decomposed in two additional sets,

$$\boldsymbol{X} = \begin{bmatrix} \boldsymbol{V} & \boldsymbol{Q} \end{bmatrix}, \tag{2.17}$$

in which the columns of $\boldsymbol{V}$ span $\boldsymbol{\nu} = range(\boldsymbol{P})$ and the columns of $\boldsymbol{Q}$ span the complementary subspace of $\boldsymbol{\nu}$ which is equal to $ker(\boldsymbol{P})$, [Griffer10].

In this thesis, only orthogonal projections are used. A projection is orthogonal if and only if $range(\boldsymbol{P})$ and $ker(\boldsymbol{P})$ are orthogonal between each other. So, using Eq. (2.13), Eq. (2.16) and Eq. (2.17), the projector $\boldsymbol{P}$ can be written as

$$\boldsymbol{P} = \boldsymbol{V} \cdot (\boldsymbol{V}^T \cdot \boldsymbol{V})^{-1} \cdot \boldsymbol{V}^T. \tag{2.18}$$

If $\boldsymbol{V}$ is orthogonal, Eq. (2.18) can be transformed into

$$\boldsymbol{P} = \boldsymbol{V} \cdot \boldsymbol{V}^T. \tag{2.19}$$

2.2.2 Eigenmodes and modal truncation

It is possible, by superposition and modal decoupling, to describe elastic response with the time of a discretized body by a linear combination of all its shape vectors.

As explained in [GimenezJalon84], analyzing the work of the elastic forces in a mechanical system, this is equal to the elastic energy stored in the system, which can only be positive or zero when the displacements of the system are rigid body displacements and there is no elastic deformation. Therefore, the stiffness matrix $\boldsymbol{K}_e$ can only be a positive definite matrix or a positive semi-definite matrix. Similarly, as a negative or zero kinetic energy makes no sense when there are non-zero velocities, the mass matrix $\boldsymbol{M}_e$ should be positive definite.

Taking into account these properties and studying the eigenproblem

$$(-\boldsymbol{M}_e\lambda_i + \boldsymbol{K}_e) \cdot \boldsymbol{\phi}_i = \boldsymbol{0}, \tag{2.20}$$

all the eigenvalues λ_i will be positive or zero, so

$$\lambda_i = \omega_i^2 \tag{2.21}$$

holds true. Taking all this into account, the eigenproblem of Eq. (2.20) can be written for all the eigenvectors at the same time:

$$\boldsymbol{K}_e \cdot \boldsymbol{\Phi} = \boldsymbol{M}_e \cdot \boldsymbol{\Phi} \cdot \boldsymbol{\Omega}, \tag{2.22}$$

$$\boldsymbol{\Phi} = \begin{bmatrix} \boldsymbol{\phi}_1 & \boldsymbol{\phi}_2 & ... & \boldsymbol{\phi}_i & ... & \boldsymbol{\phi}_N \end{bmatrix}, \tag{2.23}$$

$$\boldsymbol{\Omega} = \begin{bmatrix} \omega_1^2 & & \\ & \ddots & \\ & & \omega_N^2 \end{bmatrix}. \tag{2.24}$$

These two matrices have useful properties. As the eigenvectors are orthonormal, if scaled right, to the mass matrix and orthogonal to the stiffness matrix, it holds true

$$\boldsymbol{\Phi}^T \cdot \boldsymbol{M}_e \cdot \boldsymbol{\Phi} = \boldsymbol{E}, \tag{2.25}$$

$$\boldsymbol{\Phi}^T \cdot \boldsymbol{K}_e \cdot \boldsymbol{\Phi} = \boldsymbol{\Omega}, \tag{2.26}$$

if a new set of coordinates, called natural coordinates is defined as

$$\boldsymbol{q}_e = \boldsymbol{\Phi} \cdot \boldsymbol{q}_m \tag{2.27}$$

and premultiplied with $\boldsymbol{\Phi}^T$, then Eq. (2.4) is transformed into

$$\boldsymbol{E} \cdot \ddot{\boldsymbol{q}}_m + \boldsymbol{\Omega} \cdot \boldsymbol{q}_m = \boldsymbol{\Phi}^T \cdot \boldsymbol{f}_e. \tag{2.28}$$

It is possible to see that the original system has been decoupled and the response of the system is a combination of the different modal responses associated to each modal shape (eigenvector).

The easiest way to reduce a system is to assemble a reduction matrix with only eigenmodes in the range of the interesting eigenfrequencies. If

$$\boldsymbol{\Phi} = \begin{bmatrix} \boldsymbol{\Phi}_n & \boldsymbol{\Phi}_{N-n} \end{bmatrix} \quad \text{and} \quad \boldsymbol{q}_m = \begin{bmatrix} \boldsymbol{q}_{red} \\ \boldsymbol{q}_{N-n} \end{bmatrix}, \tag{2.29}$$

then it is possible to rewrite Eq. (2.27) into

$$\begin{aligned} \boldsymbol{q}_e &= \boldsymbol{\Phi}_n \cdot \boldsymbol{q}_{red} + \boldsymbol{\Phi}_{N-n} \cdot \boldsymbol{q}_{N-n}. \\ &\text{So,} \\ \boldsymbol{q}_e &\approx \boldsymbol{\Phi}_n \cdot \boldsymbol{q}_{red}. \end{aligned} \tag{2.30}$$

This is called modal truncation and is the easiest way to reduce the system. However, as this matrix is assembled with only eigenmodes, which represent a dynamic response, it is very difficult to obtain the static response or a response to a very low frequency excitation.

2.2.3 Component Mode Synthesis: The Craig Bampton method

The Component Mode Synthesis (CMS) technique, [CraigBampton68], was originally developed to model complex structures by dividing them into substructures

to be solved separately. To do this, the nodes of each substructure are classified into two groups: external (or boundary nodes) and internal nodes. The boundary nodes are those which are loaded, bound or interact with other substructures. With this classification Eq. (2.4) is rewritten as

$$\begin{bmatrix} \boldsymbol{M}_{ii} & \boldsymbol{M}_{ib} \\ \boldsymbol{M}_{bi} & \boldsymbol{M}_{bb} \end{bmatrix} \cdot \begin{bmatrix} \ddot{\boldsymbol{q}}_i \\ \ddot{\boldsymbol{q}}_b \end{bmatrix} + \begin{bmatrix} \boldsymbol{K}_{ii} & \boldsymbol{K}_{ib} \\ \boldsymbol{K}_{bi} & \boldsymbol{K}_{bb} \end{bmatrix} \cdot \begin{bmatrix} \boldsymbol{q}_i \\ \boldsymbol{q}_b \end{bmatrix} = \begin{bmatrix} \boldsymbol{f}_i \\ \boldsymbol{f}_b \end{bmatrix}, \tag{2.31}$$

in which the index i denotes the internal nodes. Index b indicates the set of boundary nodes.

The Craig Bampton method combines eigenmodes and some static modes in order to better catch the response of local deformations. These static or constrained modes are defined in [CraigBampton68] as the static deformation of a structure when a unit displacement is applied to one coordinate of a specific set of constrained coordinates, while the remaining coordinates of that set are constrained and the rest of the nodes of the structure are force free. In the Craig Bampton method, the set of constrained coordinates is the set of boundary coordinates. Therefore, Eq. (2.31) is transformed into

$$\begin{bmatrix} \boldsymbol{K}_{ii} & \boldsymbol{K}_{ib} \\ \boldsymbol{K}_{bi} & \boldsymbol{K}_{bb} \end{bmatrix} \cdot \begin{bmatrix} \boldsymbol{\Psi}_{ib} \\ \boldsymbol{E}_{bb} \end{bmatrix} = \begin{bmatrix} \boldsymbol{0}_{ib} \\ \boldsymbol{f}_{bb} \end{bmatrix}. \tag{2.32}$$

Transforming the Equation 2.32 the constrained mode matrix is given as

$$\boldsymbol{\Psi}_{CB} = \begin{bmatrix} \boldsymbol{\Psi}_{ib} \\ \boldsymbol{E}_{bb} \end{bmatrix} = \begin{bmatrix} -\boldsymbol{K}_{ii} \cdot \boldsymbol{K}_{ib} \\ \boldsymbol{E}_{bb} \end{bmatrix}. \tag{2.33}$$

Finally, a Craig Bampton matrix, with k boundary coordinates and $(N-k)$ external coordinates can be assembled as

$$\boldsymbol{V}_{CB} = \begin{bmatrix} \boldsymbol{\Phi}_{N-k} & \boldsymbol{\Psi}_{ib} \\ \boldsymbol{0} & \boldsymbol{E}_{bb} \end{bmatrix}, \tag{2.34}$$

in which $\boldsymbol{\Phi}_{N-k} \in \mathbb{R}^{(N-k)\times n}$ is part of the set of the $(N-k)$ fixed interface normal modes obtained by solving the eigenproblem

$$(-\boldsymbol{M}_{ii}\lambda_i + \boldsymbol{K}_{ii}) \cdot \phi_i = \boldsymbol{0} \tag{2.35}$$

and taking n from the $(N-k)$ eigenvectors to assemble one matrix $\boldsymbol{V}_{cb} \in \mathbb{R}^{N\times(n+k)}$ with $(n+k) < N$.

The Craig Bampton method is usually more powerful than modal truncation but, instead of the matrix assembled in Eq. (2.30), the Craig Bampton reduction matrix is not mass or stiffness orthogonal. Software, such as *GTM* as used in this

thesis, requires loading a reduction matrix orthogonal to the mass and stiffness matrices. Therefore in some cases it is important to orthonormalize the modes. If

$$\boldsymbol{M}_{red} = \boldsymbol{V}_{cb}^T \cdot \boldsymbol{M}_e \cdot \boldsymbol{V}_{cb} \quad \text{and} \quad \boldsymbol{K}_{red} = \boldsymbol{V}_{cb}^T \cdot \boldsymbol{K}_e \cdot \boldsymbol{V}_{cb}, \tag{2.36}$$

then, it is possible to normalize the Craig Bampton modes solving

$$\boldsymbol{K}_{red} \cdot \boldsymbol{\Phi}^* = \boldsymbol{M}_{red} \cdot \boldsymbol{\Phi}^* \cdot \boldsymbol{\Omega}^*. \tag{2.37}$$

A new set of reduced modal coordinates is defined as

$$\boldsymbol{q}_{red} = \boldsymbol{\Phi}^* \cdot \boldsymbol{q}_{red}^* \tag{2.38}$$

and the new reduction matrix yields

$$\boldsymbol{V}_{cb}^* = \boldsymbol{V}_{cb} \cdot \boldsymbol{\Phi}^*, \qquad \boldsymbol{q}_e = \boldsymbol{V}_{vb}^* \cdot \boldsymbol{q}_{red}^*. \tag{2.39}$$

It is worth mentioning that the orthogonalized eigenvectors in $\boldsymbol{\Phi}^*$ are not eigenvectors of the original system but eigenvectors of the Craig Bampton representation of the system. Therefore, a physical explanation of these vectors is more difficult but, see [CraigBampton68], the following can be said:

- Fixed boundary normal modes, as computed in Eq. (2.35), are replaced by an approximation of the eigenvectors of the unconstrained body. Out of these modes, 6 are usually the rigid body modes.

- Constrained modes are replaced with a *boundary eigenvector*, a concept best illustrated by comparing the modes and after orthogonalization of a rectangular plate which has Craig Bampton boundary points along one of its long edges. The Craig Bampton mode in Fig. 2.2 featured a unit displacement of one of its edge nodes; all the other nodes of the edge being fixed. After orthonormalization, we see modes like the one depicted in Fig. 2.3 which has a sinusoidal curve along the boundary.

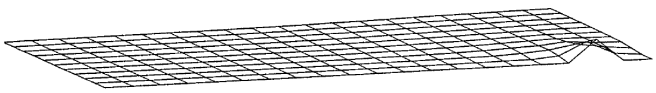

Figure 2.2: Representation of a Craig Bampton constrained mode.

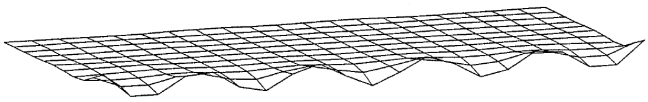

Figure 2.3: Schematic representation of a boundary mode.

2.2.4 Dynamic condensation

Dynamic condensation is a generalization of the static one, used for example to compute the static modes in the Craig Bampton reduction method. If the mechanical system is expressed as a control system it is possible to write

$$\begin{aligned} \boldsymbol{M}_e \cdot \ddot{\boldsymbol{q}}_e + \boldsymbol{K}_e \cdot \boldsymbol{q}_e &= \boldsymbol{B}_e \cdot \boldsymbol{u}, \\ \boldsymbol{y} &= \boldsymbol{C}_e \cdot \boldsymbol{q}_e, \end{aligned} \tag{2.40}$$

where $\boldsymbol{u}$ are the inputs to the system ($\boldsymbol{f}_e = \boldsymbol{B}_e \cdot \boldsymbol{u}$) and $\boldsymbol{y}$ are displacements of interest extracted via matrix $\boldsymbol{C}_e$. The mechanical impedance of the system, see [Balmes05], can be expressed as

$$\boldsymbol{Z}(\omega) = -\omega^2 \boldsymbol{M} + \boldsymbol{K}. \tag{2.41}$$

If a transformation matrix $\boldsymbol{T}$ is given such that

$$\boldsymbol{q}_e = \boldsymbol{T} \cdot \boldsymbol{q}_b \tag{2.42}$$

holds true, an analogy with the constrained modes calculation is established

$$\begin{bmatrix} \boldsymbol{Z}_{ii} & \boldsymbol{Z}_{ib} \\ \boldsymbol{Z}_{bi} & \boldsymbol{Z}_{bb} \end{bmatrix} \cdot \begin{bmatrix} \boldsymbol{\Theta}_{ib} \\ \boldsymbol{E}_{bb} \end{bmatrix} = \begin{bmatrix} \boldsymbol{0}_{ib} \\ \boldsymbol{f}_{bb} \end{bmatrix} \tag{2.43}$$

and the transformation matrix $\boldsymbol{T}$ can be expressed as

$$\boldsymbol{T} = \begin{bmatrix} \boldsymbol{\Theta}_{ib} \\ \boldsymbol{E}_{bb} \end{bmatrix} = \begin{bmatrix} -\boldsymbol{Z}_{ii}^{-1} \cdot \boldsymbol{Z}_{ib} \\ \boldsymbol{E}_{bb} \end{bmatrix}. \tag{2.44}$$

These new modes contained in $\boldsymbol{T}$ can be assembled in a more general reduction matrix in a similar fashion to the Craig Bampton reduction matrix (Eq. (2.33), Eq. (2.34), and Eq. (2.35))

$$\boldsymbol{V}_{dc} = \begin{bmatrix} \boldsymbol{\Phi}_{N-k} & \boldsymbol{\Theta}_{ib} \\ \boldsymbol{0} & \boldsymbol{E}_{bb} \end{bmatrix}. \tag{2.45}$$

2.2.5 CMS-Gram reduction method

One of the major drawbacks of the modal truncation and the Craig Bampton reduction techniques is that it is usually difficult to determine the most relevant modes in order to assemble the reduction matrix. As proposed by [HolzwarthEberhard], the decomposition in Gramian matrices enables one to rank the importance of the deformation patterns from an energy point of view. The controllability and observability matrices, $\boldsymbol{P}$, $\boldsymbol{Q}$, are related to the excitation energies (how much energy is needed to excite one state of the system) and output energy (how much energy it is possible to observe at one output of the system), respectively.

According to [HolzwarthEberhard], a quantification of system properties from this point of view can be expressed with the system invariant Hankel Singular Values (HSV), σ_i, defined as square roots of the spectrum of the product of $\boldsymbol{P}$ and $\boldsymbol{Q}$

$$\sigma_i := \sqrt{\lambda_i(\boldsymbol{P}\cdot\boldsymbol{Q})}, \quad \text{with } (\boldsymbol{P}\cdot\boldsymbol{Q})\cdot\boldsymbol{\chi} = diag(\lambda_i)\cdot\boldsymbol{\chi}, \quad i = 1, ..., N. \tag{2.46}$$

The transformation matrix $\boldsymbol{T}$ needed to obtain this representation is calculated with two Cholesky decompositions and a singular value decomposition, SVD. For symmetric systems, the observability and controllability matrices are identical and the transformation matrix $\boldsymbol{T}$ can be obtained solving the eigenproblem

$$\boldsymbol{P}\cdot\boldsymbol{T} = diag(\xi_i)\cdot\boldsymbol{T}, \tag{2.47}$$

where the eigenvalues are equivalent to the Henkel singular value (HSV), e.g. $\xi_i = \sigma_i$, of the system. If the eigenvectors are sorted according to the HSV in descending order and the first n are chosen to assemble the reduction matrix $\boldsymbol{V}$ this is equivalent to eliminating those states of the system which are difficult to excite or are difficult to observe. Therefore, the problem of determining which modes are more important in the system is greatly reduced.

There are several definitions for Gramian matrices for second order systems. In [HolzwarthEberhard] if

$$\boldsymbol{L}(\omega) = -\omega^2\boldsymbol{M}_e + i\omega\boldsymbol{D}_e + \boldsymbol{K}_e, \tag{2.48}$$

the Gramian matrices are defined as

$$\boldsymbol{P}_p = \frac{1}{2\pi}\int_{-\infty}^{+\infty} \boldsymbol{L}^{-1}(\omega)\cdot\boldsymbol{B}_e\cdot\boldsymbol{B}_e^t\cdot\boldsymbol{L}^{-H}(\omega)\mathrm{d}\omega, \tag{2.49}$$

$$\boldsymbol{Q}_{pv} = \frac{1}{2\pi}\int_{-\infty}^{+\infty} \boldsymbol{L}^{-H}(\omega)\cdot\boldsymbol{C}_e^t\cdot\boldsymbol{C}_e\cdot\boldsymbol{L}^{-1}(\omega)\mathrm{d}\omega, \tag{2.50}$$

where $\boldsymbol{B}_e$ and $\boldsymbol{C}_e$ are the input and observation matrix from Eq. (2.40)

For mechanical applications, the behavior of the system is usually interesting for a special range of frequencies. In these cases it is possible to define the Gramian matrices as

$$\boldsymbol{P}_p = \frac{1}{\pi}\int_{\omega_1}^{\omega_2} \boldsymbol{L}^{-1}(\omega)\cdot\boldsymbol{B}_e\cdot\boldsymbol{B}_e^t\cdot\boldsymbol{L}^{-H}(\omega)\mathrm{d}\omega. \tag{2.51}$$

The main drawback of Gramian matrices-based reduction techniques is the computational effort needed to compute the Gramian matrices and they are usually not computed exactly but approximately.More research has been done in [LehnerEberhard07] and [FehrLehnerEberhard07].

2.2.6 *MatMorembs*

Before creating a reduction matrix, *MatMorembs* needs to build a standard data structure with all the relevant information of the system. To do this, it is necessary to provide the software with three files:

- *system*.fil, which contains the information about the modes and the mesh of the model.
- *system*_MASS.mtx, which contains the mass matrix of the system.
- *system*_STIF.mtx, which contains the stiffness matrix of the system.

Listing 2.1: Modifications of the imput file required to obtain the mass and stiffness matrices and the modal information.

```
1  **-----------------------------------------------------
2  *Step, name=Step-0
3  *matrix generate, stiffness, mass
4  *matrix output, stiffness, mass
5  *End Step
6  **-----------------------------------------------------
7  *Step, name=Step-1, perturbation
8  *Frequency, eigensolver=Lanczos, acoustic coupling=on,
      normalization=mass, bias=1.
9  Number of Eigenmodes, Inital Eigenmode, , , ,
10 ...
11 *Node file
12 u
13 *End Step
```

These files are provided via Abaqus running a modified version of the model input file. In this file some code lines need to be added, presented in the Listing 2.1, before running the simulation again. Once the simulation is completed the three files described above will be available. By running the functions *abaqus_to_matlab* and *femdata_to_systemdata* in *MatMorembs* a database containing all the information of the system is created. When the data structure *sysdata* is generated it is possible to run all the reduction functions.

The *sysdata* structure stores information such as the mass matrix, stiffness matrix and damping matrix (if defined), mode matrix and their related frequencies. All this information is stored for the free model (without restriction) with a dimension of $\hat{N}$ DOF and for the constrained model, whose dimension is N DOF. Later, when the reduction matrix is assembled, it is exported to *GTM*.

A post processing step is needed because the model used to compute these matrices is the bounded model, and *GTM* needs matrices with the full system dimension. This information is stored in a constraint matrix, $\boldsymbol{T}_c$ defined in such a way that if $\{\boldsymbol{M}_{con},\ \boldsymbol{K}_{con}\}$ are the matrices of the constrained system, and $\{\boldsymbol{M}_{free},\ \boldsymbol{K}_{free}\}$ are the matrices of the free system, then

$$\{\boldsymbol{M}_{con},\ \boldsymbol{K}_{con}\} = \boldsymbol{T}_c^T \cdot \{\boldsymbol{M}_{free},\ \boldsymbol{K}_{free}\} \cdot \boldsymbol{T}_c \tag{2.52}$$

holds true. So, if the reduction matrices for the full and the constrained system are $\boldsymbol{V}_{free}$ and $\boldsymbol{V}_{con}$ respectively then

$$\boldsymbol{V}_{free} = \boldsymbol{T}_c \cdot \boldsymbol{V}_{con} \tag{2.53}$$

holds. Therefore it is possible to transform the reduction matrix easily.

Another extra preprocessing step related to numerical difficulties is also needed. Sometimes the modes used are almost linearly dependent and as a consequence numerical problems occur. An orthogonalization process of one set of modes with another (e.g. the dynamic modes and the normal modes) of the reduction matrix seem to solve that problem.

Finally, to fulfill the other two conditions (i.e. being mass and stiffness orthogonal), the orthonormalised reduction matrix should be decoupled. To do this, the function *decouple_system.m* is implemented in *MatMorembs*. Again, some numerical problems may occur when elements in the reduced matrices, with non zero and not negligible values, appear outside the diagonal. The function was modified to disregard those elements, so outside the main diagonal of the mass and stiffness matrix only zeros or elements with a very low value appear.

2.3 Mechanical contact theory

In order to study contact dynamics it is necessary to proceed in two steps. One to determine whether the contact has been produced or not, see Section 2.3.1 and another consecutive step to compute the interaction, in the form of a contact force acting between two bodies. In this thesis, the penalty method has been used (Section 2.3.2) to model these forces. It is possible to model the interaction between contact surfaces with or without friction. In the case of frictional contact, tangential forces will appear on the contact surfaces. In this work only contact without friction is considered. Thus only forces normal to the contact surfaces can be expected.

2.3.1 Contact mechanics

As explained in [SeifriedSchiehlenEberhard10], if $\mathbf{\Gamma}_I$ represents the whole surface of the first body and $\mathbf{\Gamma}_{II}$ the surface of the second body, then for every possible pair of points $\boldsymbol{P}_i^I \in \mathbf{\Gamma}_I$ and $\boldsymbol{P}_i^{II} \in \mathbf{\Gamma}_{II}$ it is possible to define two reference frames attached to each point $\{\boldsymbol{P}_i,\ \boldsymbol{n}_i,\ \boldsymbol{t}_{1i},\ \boldsymbol{t}_{2i}\}$, where vectors $\boldsymbol{t}_{1i}$ and $\boldsymbol{t}_{2i}$ define a plane tangential to the surface $\mathbf{\Gamma}$ at point $\boldsymbol{P}_i$ and $\boldsymbol{n}_i$ is the surface normal vector (pointing outside) at point $\boldsymbol{P}_i$.
If two points $\boldsymbol{P}^I$ and $\boldsymbol{P}^{II}$ are determined in such a way that they yield the smallest normal distance of all surface points, then the distance vector $\boldsymbol{g}$, from $\boldsymbol{P}^I$ to $\boldsymbol{P}^{II}$ is normal to both tangential planes. In this case the smallest distance in normal direction is given as

$$g_N = \boldsymbol{n}_I^T \cdot \boldsymbol{g} = -\boldsymbol{n}_{II}^T \cdot \boldsymbol{g} = \boldsymbol{n}_I^T \cdot (\boldsymbol{r}_{OP^{II}} - \boldsymbol{r}_{OP^I}), \tag{2.54}$$

where $\boldsymbol{r}_{OP^I}$ and $\boldsymbol{r}_{OP^{II}}$ are the position vectors of $\boldsymbol{P}^I$ and $\boldsymbol{P}^{II}$ in the inertial reference frame. Using Eq. (2.54), three situations can be differed:

$$g_N = \begin{cases} > 0 & \text{No contact} \\ = 0 & \text{Contact} \\ < 0 & \text{Penetration} \end{cases} . \tag{2.55}$$

Differentiating g_N it is possible to obtain the relative velocity between the bodies

$$\dot{g}_N = \boldsymbol{n}_I^T \cdot (\boldsymbol{J}_{P^{II}} - \boldsymbol{J}_{P^I}) \cdot \dot{\boldsymbol{y}} + \boldsymbol{n}_I^T \cdot (\boldsymbol{v}_{P^{II}} - \boldsymbol{v}_{P^I}), \tag{2.56}$$

where $\dot{\boldsymbol{y}}$ are the generalized velocities, $\boldsymbol{J}$ are the Jacobian matrices evaluated at points $\boldsymbol{P}^I$ and $\boldsymbol{P}^{II}$ and $\boldsymbol{v}$ are their local velocities.These local velocities only appear in rheonomic systems, see [SeifriedSchiehlenEberhard10]. If $\dot{g}_N < 0$, the bodies move towards each other and contact can occur.

2.3.2 Penalty factor

In order to model the contact interaction, different strategies could be used. In this work, the penalty factor approach is selected. With this technique the contact force is proportional to the penetration distance of one point of a body into the surface of another. The proportionality factor is called contact penalty factor. So the normal force can be expressed as

$$\boldsymbol{F}_N = \begin{cases} c_p \boldsymbol{n} g & \text{if} \quad g \leq 0 \\ 0 & \text{if} \quad g > 0 \end{cases} \tag{2.57}$$

where c_p is the contact penalty factor and $\boldsymbol{n}$ is a normal vector to the surface. The potential energy of an elastic body without contact interaction between the bodies can be expressed as (see [BednarekKowalczyk11])

$$\Pi = \frac{1}{2}\boldsymbol{q}_e^T \cdot \boldsymbol{K}_e \cdot \boldsymbol{q}_e - \boldsymbol{q}_e^T \cdot \boldsymbol{f}_e \tag{2.58}$$

where $\boldsymbol{q}_e$ represents the nodal coordinates of the elastic body, $\boldsymbol{K}_e$ is the stiffness matrix and $\boldsymbol{f}_e$ the external forces acting on the body. If a contact in only one node appears, Eq. (2.58) is transformed into

$$\Pi = \frac{1}{2}\boldsymbol{q}_e^T \cdot \boldsymbol{K}_e \cdot \boldsymbol{q}_e - \boldsymbol{q}_e^T \cdot \boldsymbol{f}_e + \frac{1}{2}\boldsymbol{g}_N^T \cdot c_p \boldsymbol{g}_N, \tag{2.59}$$

where $\boldsymbol{g}_N$ is the distance vector defined in Eq. (2.54) and c_p is the contact penalty factor that Eq. (2.57) verifies. In the case of this work, when there is contact interaction no external forces will be applied, so Eq. (2.59) is transformed into

$$\Pi = \frac{1}{2}\boldsymbol{q}_e^T \cdot \boldsymbol{K}_e \cdot \boldsymbol{q}_e + \frac{1}{2}\boldsymbol{g}_N^T \cdot c_p \boldsymbol{g}_N = \Pi_{nc} + \boldsymbol{q}_e + \frac{1}{2}\boldsymbol{g}_N^T \cdot c_p \tag{2.60}$$

and minimizing the potential energy, see [BednarekKowalczyk11], yields

$$\frac{\partial \Pi_{nc}}{\partial \boldsymbol{q}_e} + c_p \boldsymbol{g}_N \cdot \frac{\partial \boldsymbol{g}_N}{\partial \boldsymbol{q}_e} = \boldsymbol{0}. \tag{2.61}$$

It is possible to see in the equation the effect of the penalty factor. A small penalty factor implies that the first term of Eq. (2.61) gains importance and it results in large penetrations, which are physically not real. The bigger the penalty factor, the smaller the penetration, and the system will converge to a solution closer to reality. However, increasing the penalty factor over a certain limit may have some negative consequences.

Going deep into analyzing the penalty contact effect in the accuracy of the solution, research was performed in [Nour-OmidWriggers87]. The contact condition can be expressed with a set of linear constraint equations as

$$\boldsymbol{B}^T \cdot \boldsymbol{q} = \boldsymbol{u}, \tag{2.62}$$

where $\boldsymbol{B}$ is an $m \times N$ matrix. With Eq. (2.62) it is possible to rewrite Eq. (2.60) as:

$$\Pi_c = \Pi_{nc} + \frac{c_p}{2}[(\boldsymbol{B}^T \cdot \boldsymbol{q} - \boldsymbol{u})^T \cdot (\boldsymbol{B}^T \cdot \boldsymbol{q} - \boldsymbol{u})] \tag{2.63}$$

and minimizing the potential energy, it yields to

$$(\boldsymbol{K} + c_p \boldsymbol{B} \cdot \boldsymbol{B}^T) \cdot \boldsymbol{q} = c_p \boldsymbol{B} \cdot \boldsymbol{u}, \tag{2.64}$$

$$\boldsymbol{K}_{mod} = \boldsymbol{K} + c_p \boldsymbol{B} \cdot \boldsymbol{B}^T \tag{2.65}$$

In Eq. (2.65) the modified stiffness matrix remains symmetric and positive definite but its structure depends on the value of the c_p. As stated in [Nour-OmidWriggers87], there are two sources of error that affect the accuracy based on the penalty method. Both errors depend strongly on the penalty parameter, but in two different ways. The first error was mentioned before: small penalty parameters badly enforce the constraint equations. In fact, the exact solution will only be obtained when $c_p \to \infty$. If the solution of Eq. (2.64) is computed, then

$$\boldsymbol{q} = [\boldsymbol{K}^{-1} - c_p \boldsymbol{K}^{-1} \cdot \boldsymbol{B} \cdot (\boldsymbol{E} + c_p \boldsymbol{B}^T \cdot \boldsymbol{K}^{-1} \cdot \boldsymbol{B})^{-1} \cdot \boldsymbol{B}^T \cdot \boldsymbol{K}^{-1}] \cdot c_p \boldsymbol{B} \cdot \boldsymbol{u} \tag{2.66}$$

and the exact solution is

$$\boldsymbol{q}_E = \boldsymbol{K}^{-1} \cdot \boldsymbol{B} \cdot (\boldsymbol{B}^T \cdot \boldsymbol{K}^{-1} \cdot \boldsymbol{B})^{-1} \cdot \boldsymbol{u}. \tag{2.67}$$

To estimate the error, in [Nour-OmidWriggers87] the following expression is proposed, retaining only terms of order $1/c_p$

$$\boldsymbol{q} - \boldsymbol{q}_E \approx \frac{1}{c_p} \boldsymbol{K}^{-1} \cdot \boldsymbol{B} \cdot (\boldsymbol{B}^T \cdot \boldsymbol{K}^{-1} \cdot \boldsymbol{B})^{-1} \cdot (\boldsymbol{B}^T \cdot \boldsymbol{K}^{-1} \cdot \boldsymbol{B})^{-1} \cdot (-\boldsymbol{u}) \tag{2.68}$$

and taking norms

$$\begin{aligned} \|\boldsymbol{q} - \boldsymbol{q}_E\| &\approx \frac{1}{c_p} \|\boldsymbol{K}^{-1} \cdot \boldsymbol{B} \cdot (\boldsymbol{B}^T \cdot \boldsymbol{K}^{-1} \cdot \boldsymbol{B})^{-1} \cdot (\boldsymbol{B}^T \cdot \boldsymbol{K}^{-1} \cdot \boldsymbol{B})^{-1} \cdot (-\boldsymbol{u})\| \\ &\leq \underbrace{\frac{\|(\boldsymbol{B}^T \cdot \boldsymbol{K}^{-1} \cdot \boldsymbol{B})^{-1}\|}{c_p}}_{1} \underbrace{\|\boldsymbol{K}^{-1} \cdot \boldsymbol{B} \cdot (\boldsymbol{B}^T \cdot \boldsymbol{K}^{-1} \cdot \boldsymbol{B})^{-1} \cdot (\boldsymbol{u})\|}_{2}. \end{aligned} \tag{2.69}$$

In Eq 2.69, 2 is the contribution to $\boldsymbol{q}_E$ due to the contact forces and it can be assumed equal to $c\|\boldsymbol{q}_E\|$. Here, c is a constant and can be considered the unity in most cases. Then

$$\frac{\|\boldsymbol{q} - \boldsymbol{q}_E\|}{\|\boldsymbol{q}_E\|} \leq \frac{c\|(\boldsymbol{B}^T \cdot \boldsymbol{K}^{-1} \cdot \boldsymbol{B})^{-1}_{)}\|}{c_p} \tag{2.70}$$

measures the first error. The second source of error is due to the loss of information when a larger quantity is added to a small one in the computer. Representing the example in [Nour-OmidWriggers87], if a coefficient k of the stiffness matrix $\boldsymbol{K}$ is $k = 1/3$, in an environment with 8 digits of accuracy, it is represented as $k = 0.33333333$. If a penalty parameter, $c_p = 10^3$ is added to this term the result is 0.10003333×10^4 and half of the digits in k are lost. Such errors are studied in [Wilkinson63] and are bounded by

$$\frac{\|\boldsymbol{q} - \boldsymbol{q}_E\|}{\|\boldsymbol{q}_E\|} \leq n\epsilon\frac{c_p}{k}. \tag{2.71}$$

In Eq. (2.71) it is possible to see that the larger the c_p the larger the error may be. If the c_p is too large, small perturbations in the initial conditions can lead to large differences in the solution, i.e., the larger the penalty factor, the worse the modified stiffness matrix $\boldsymbol{K}_{mod}$ is conditioned.

2.3.3 *GTM*

GTM is divided basically into three modules: two pre-processing functions and then, the integration skin. The first preprocessing function, called *gtm_prep_1*, reads the *Abaqus* input file and stores the geometry of the model, with all the nodal information (i.e. nodal position, nodes contained in the flanks, bore nodes...). *GTM* will establish a kinematic coupling condition between the reference frame and the bore nodes. It also writes an *Abaqus* input file in order to compute the modal matrix and the vector of eigenfrequencies associated to each mode. In a similar way as the procedure to import to *MatMorembs*, the new input file is run in *Abaqus* and the .fil, MASS.mtx and STIF.mtx are created.

The function *gtm_prep_2* will read these matrices and with all the information (geometry, mass and stiffness matrices and modal matrices) will determine all the standard data needed to assemble the movement equations. If a reduction matrix should be loaded, the modal matrix data file must be substituted by the reduction matrix file.

Once the preprocessing is finished, it is possible to set up the model determining its initial position, how it is bounded and the initial conditions for integration. *GTM* uses a standard integrator from *Matlab*, in this case the *@ode45*. This integrator can solve equations with the form

$$\dot{\boldsymbol{x}} = f(t,\ \boldsymbol{x}), \tag{2.72}$$

so the original equation of motion (Eq. (2.9)) described in Chapter 2 should be modified and adapted. The new state variable, $\boldsymbol{x}$ is defined as

$$\boldsymbol{x}^T = \begin{bmatrix} \boldsymbol{r} & \boldsymbol{p} & \boldsymbol{q}_{red} & \boldsymbol{v} & \boldsymbol{\omega} & \dot{\boldsymbol{q}}_{red} \end{bmatrix} \quad \text{and}$$
$$\dot{\boldsymbol{x}}^T = \begin{bmatrix} \dot{\boldsymbol{r}} & \dot{\boldsymbol{p}} & \dot{\boldsymbol{q}}_{red} & \dot{\boldsymbol{v}} & \dot{\boldsymbol{\omega}} & \ddot{\boldsymbol{q}}_{red} \end{bmatrix}.$$

All the variables stored in $\boldsymbol{x}$ and their derivatives are projected in the reference frame, so after integration, a base change to the inertial frame (whose origin is at $\boldsymbol{O}_I = \boldsymbol{0}$) is performed. Vector $\boldsymbol{r}$ represents the position of the origin of the reference frame, $\boldsymbol{v}$ and $\boldsymbol{\omega}$ are the translational and rotational velocities with respect to the inertial frame. Vector $\boldsymbol{p}$ represent the quaternions of the body and finally $\boldsymbol{q}_{red}$ are the reduced elastic coordinates.

2.3.4 *GTM* contact algorithm

The contact routine in *GTM* can be approached in two steps: one to determine which teeth are in contact and a second to compute the contact force. The first part of the routine starts to resolve which tooth from one gear is closer to the center of the other gear. This is solved by computing the distance from the node closest to the center of gravity of each tooth to the center of the other gear. Once this tooth has been obtained, the contact candidates are selected. The way these candidates are selected is determined by the user in the model setup script.

From here on, in order to improve computational efficiency, the software takes into account only the nodes of the candidate teeth. The second step is to establish the positions and the velocities of the candidate nodes. Velocities are needed in case frictional contact is considered, which is not the scope of this thesis. The deformed state of the nodes is computed with the help of the modal matrix and the values of the modal coordinates. As the linear and angular velocities of the reference frame are computed in every integration step, once the position of the nodes is determined, velocity computation is straightforward.

Having completed this preliminary step, the contact routine starts a loop over all the candidate teeth to detect where the collision occurs in the first place. One surface, right or left, of one tooth is chosen and its counterpart from the other gear is selected. Depending on the weighting factor wf, the roles of master and slave surfaces is assigned:

- if $wf = 1$ the surface from first gear is selected as master surface.
- if $wf = 0$ the surface from first gear is selected as slave surface.
- for $wf \in (0, 1)$ each surface acts as an master and slave surface. The result is computed by weighting both results obtained: if $\boldsymbol{f}_c^I$ is the contact force setting the first surface as master surface and $\boldsymbol{f}_c^{II}$ is the force with the first surface acting as the slave surface, the contact force will be computed as $\boldsymbol{f}_c = wf\boldsymbol{f}_c^I + (1 - wf)\boldsymbol{f}_c^{II}$

By definition, one node contained in the slave surface tries to penetrate the master surface. The real continuous, geometrical surface is approximated in the

model by a determined number of squared faces defined by its apex nodes. To resolve whether a slave node can penetrate the surface, a bounding sphere test is performed. In this test each face is surrounded by a sphere whose center is located at the geometric mid-point of the face and the radius is the maximal distance from the mid-point to the apex nodes. If the slave node is not within this distance another node will be considered until one stands inside the sphere. If no slave node satisfies this condition, the same procedure is repeated with another face.

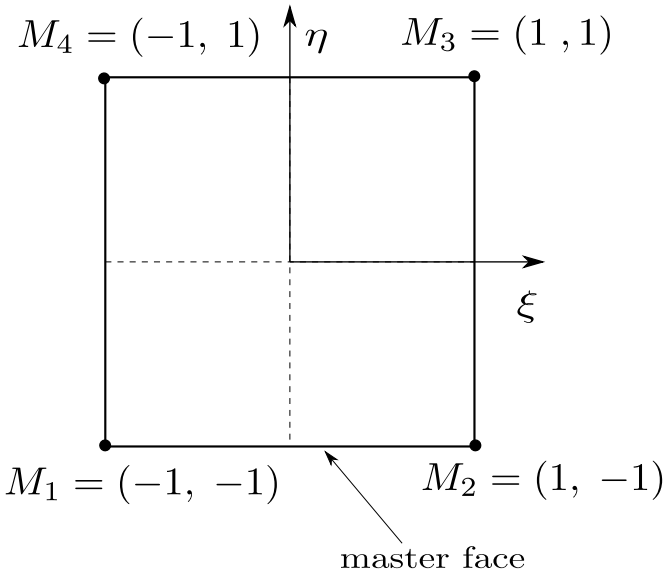

Figure 2.4: Domain of the ξ, η parametrization.

Once a slave node satisfies the bounding sphere condition, the penetration point should be calculated. To do this, the master face is parameterized in the following way, see Fig 2.4,

$$\begin{aligned} \varphi: \quad & \mathbb{R}^2 \quad \longrightarrow \quad \mathbb{R}^3 \\ [\xi,\ \eta] \in [0,\ 1] \times [0,\ 1] \quad & \rightarrow \quad \boldsymbol{f}(\xi,\ \eta). \end{aligned} \tag{2.73}$$

The function $\boldsymbol{f} \in \mathbb{R}^{1\times 3}$ is different for each face considered and can be written with the help of an ansatz function $\hat{\boldsymbol{A}} \in \mathbb{R}^{1\times 4}$

$$\boldsymbol{f} = \boldsymbol{u} = \hat{\boldsymbol{A}} \cdot \hat{\boldsymbol{u}}^T, \tag{2.74}$$

where $\boldsymbol{u}$ is the position vector of one point of the face and $\hat{\boldsymbol{u}}$ is the matrix assembled with the position vectors of the apex nodes.

$$\hat{\boldsymbol{u}} = \begin{bmatrix} \boldsymbol{u}_1 & \dots & \boldsymbol{u}_4 \end{bmatrix}. \tag{2.75}$$

If Equation 2.74 holds true, see [Eberhard00], the ansatz function $\hat{\boldsymbol{A}}$ is defined as:

$$\begin{aligned} A(1) &= \frac{1}{4}(1+\xi)(1+\eta) \qquad A(2) = \frac{1}{4}(1-\xi)(1+\eta) \\ A(3) &= \frac{1}{4}(1-\xi)(1-\eta) \qquad A(4) = \frac{1}{4}(1+\xi)(1-\eta) \end{aligned} \tag{2.76}$$

and

$$\hat{\boldsymbol{A}} = \begin{bmatrix} A(1) & \dots & A(4) \end{bmatrix}. \tag{2.77}$$

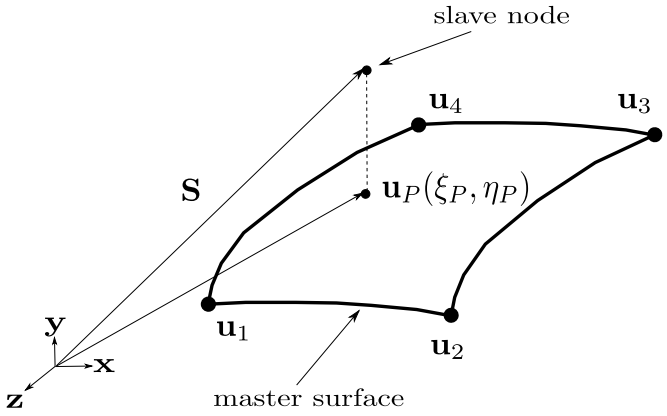

Figure 2.5: Penetration point and slave node.

The penetration point (see Fig. 2.5), $\boldsymbol{u}_p(\xi_p,\ \eta_p) = \boldsymbol{f}^T(\xi_p,\ \eta_p)$, is defined as the point of the surface closest to the slave node defined by its position vector $\boldsymbol{S} \in \mathbb{R}^{3\times 1}$. Therefore $\boldsymbol{u}_p$ is the normal projection of $\boldsymbol{S}$ onto the surface, mathematically

$$F_1(\xi,\ \eta) = \frac{\partial \boldsymbol{f}}{\partial \xi}[\boldsymbol{S} - \boldsymbol{f}^T(\xi,\ \eta)] = 0 \ \text{ and } \quad F_2(\xi,\ \eta) = \frac{\partial \boldsymbol{f}}{\partial \eta}[\boldsymbol{S} - \boldsymbol{f}^T(\xi,\ \eta)] = 0, \tag{2.78}$$

where $\frac{\partial \boldsymbol{f}}{\partial \xi}$ and $\frac{\partial \boldsymbol{f}}{\partial \eta}$ are the two vectors tangent to the surface at the point $\boldsymbol{u}_p$.

GTM will use the Newton algorithm to approximate a solution of Eq. (2.78). If $\boldsymbol{X} = [\xi,\ \eta]^T$ and $\boldsymbol{F} = [F_1,\ F_2]^T$, then, the numerical problem can be expressed as

$$\begin{aligned} \boldsymbol{X}_0 &= [0,\ 0]^T \\ \boldsymbol{X}_n &= \boldsymbol{X}_{n-1} - \boldsymbol{J}_{\boldsymbol{F}}^{-1}(\boldsymbol{X}_{\boldsymbol{n-1}}) \cdot \boldsymbol{F}(\boldsymbol{X}_{n-1}) \end{aligned} \tag{2.79}$$

From Equation 2.78 the Jacobian matrix can be assembled

$$\boldsymbol{J_F} = \begin{bmatrix} -\frac{\partial \boldsymbol{f}}{\partial \xi}(\frac{\partial \boldsymbol{f}}{\partial \xi})^T & \frac{\partial \boldsymbol{f}^2}{\partial \xi \partial \eta}(\boldsymbol{S} - \boldsymbol{f}^T) - \frac{\partial \boldsymbol{f}}{\partial \xi}(\frac{\partial \boldsymbol{f}}{\partial \eta})^T \\ \frac{\partial \boldsymbol{f}^2}{\partial \eta \partial \xi}(\boldsymbol{S} - \boldsymbol{f}^T) - \frac{\partial \boldsymbol{f}}{\partial \eta}(\frac{\partial \boldsymbol{f}}{\partial \xi})^T & -\frac{\partial \boldsymbol{f}}{\partial \eta}(\frac{\partial \boldsymbol{f}}{\partial \eta})^T \end{bmatrix}. \tag{2.80}$$

As $\boldsymbol{f} = \hat{\boldsymbol{A}} \cdot \hat{\boldsymbol{u}}$ and $\hat{\boldsymbol{u}}$ is invariant during each integration step, the derivatives of $\boldsymbol{f}$ are the derivatives of $\hat{\boldsymbol{A}}$, which are easily obtained, multiplying by $\hat{\boldsymbol{u}}$

After the penetration point has been computed, it only remains to calculate and store the contact force and torques. The normal vector to the surface at $\boldsymbol{u}_p$ is defined as

$$\boldsymbol{n} = \frac{\frac{\partial \boldsymbol{f}}{\partial \xi} \times \frac{\partial \boldsymbol{f}}{\partial \eta}}{\| \frac{\partial \boldsymbol{f}}{\partial \xi} \times \frac{\partial \boldsymbol{f}}{\partial \eta} \|} \tag{2.81}$$

and finaly the force acting on the slave node will be computed

$$\boldsymbol{F}_s = \boldsymbol{n} g_N c_p \tag{2.82}$$

if the penetration g_N is negative. The contact force reacts on the master face with the same force acting in opposite direction. This force is distributed at the four nodes that define the contact face proportionally to the ansatz function evaluated at penetration point:

$$\boldsymbol{F}_i = \boldsymbol{F} \cdot \hat{\boldsymbol{A}}(i)(\xi_p,\ \eta_p), \quad i = 1,\ ...\ 4. \tag{2.83}$$

2.4 Stress recovery

It is possible to recover the stress of an arbitrary point of the body $\boldsymbol{P}$, in a similar fashion as the nodal displacements are computed. If $[\boldsymbol{\sigma}](\boldsymbol{P})$ is the stress tensor at point $\boldsymbol{P}$

$$[\boldsymbol{\sigma}](\boldsymbol{P}) = \begin{bmatrix} \sigma_{11} & \tau_{12} & \tau_{13} \\ \tau_{21} & \sigma_{22} & \tau_{23} \\ \tau_{31} & \tau_{32} & \sigma_{33} \end{bmatrix}, \quad \text{where} \quad \tau_{ij} = \tau_{ji} \ \ \forall i \neq j, \tag{2.84}$$

its elements can be rearranged in a vector

$$\boldsymbol{\sigma}(\boldsymbol{P}) = \begin{bmatrix} \sigma_{11} & \sigma_{12} & \sigma_{33} & \tau_{12} & \tau_{13} & \tau_{23} \end{bmatrix}^T. \tag{2.85}$$

The objective is to relate this vector with the elastic coordinates vector $\boldsymbol{q}_e$. The longitudinal, $[\epsilon_{11},\ \epsilon_{22},\ \epsilon_{33}]^T$ and shear strains, $[\gamma_{12},\ \gamma_{13},\ \gamma_{23}]^T$ are related to the

elastic deformation $\boldsymbol{u}(\boldsymbol{P}) = [u_1,\ u_2,\ u_3]^T$ in the following way

$$\boldsymbol{\epsilon}(\boldsymbol{P}) = \boldsymbol{D}\cdot\boldsymbol{u}(\boldsymbol{P}) = \begin{bmatrix}\epsilon_{11}\\ \epsilon_{22}\\ \epsilon_{33}\\ \gamma_{12}\\ \gamma_{13}\\ \gamma_{23}\end{bmatrix} = \begin{bmatrix}\partial/\partial x & & \\ & \partial/\partial y & \\ & & \partial/\partial z\\ \partial/\partial y & \partial/\partial x & \\ \partial/\partial z & & \partial/\partial x\\ & \partial/\partial z & \partial/\partial y\end{bmatrix}\cdot\begin{bmatrix}u_1\\ u_2\\ u_3\end{bmatrix}. \tag{2.86}$$

With the generalized Hooke's law it is possible to relate the strains and the stresses, in the linear elastic phase, with a material matrix $\boldsymbol{H}$

$$\boldsymbol{\epsilon} = \boldsymbol{H}\cdot\boldsymbol{\sigma}. \tag{2.87}$$

Combining Eq. (2.86) and Eq. (2.87) yields to

$$\boldsymbol{\sigma}(\boldsymbol{P}) = \boldsymbol{H}^{-1}\cdot\boldsymbol{D}\cdot\boldsymbol{u}(\boldsymbol{P}) = \boldsymbol{H}^{-1}\cdot\boldsymbol{D}\cdot\boldsymbol{\Phi}_R(\boldsymbol{P})\cdot\boldsymbol{q}_e. \tag{2.88}$$

$$\text{If}\quad \boldsymbol{\Upsilon}_s(\boldsymbol{P}) = \boldsymbol{H}^{-1}\cdot\boldsymbol{D}\cdot\boldsymbol{\Phi}_R(\boldsymbol{P}),\quad \text{then,}\quad \boldsymbol{\sigma}(\boldsymbol{P}) = \boldsymbol{\Upsilon}_s(\boldsymbol{P})\cdot\boldsymbol{q}_e, \tag{2.89}$$

where $\boldsymbol{\Upsilon}_s(\boldsymbol{P})$ is the stress modal matrix and $\boldsymbol{\Phi}_R(\boldsymbol{P})$ is the modal matrix that relate the elastic deformations of the continuum body with the elastic coordinates, following the Ritz approach, Eq. (2.2)). Equation 2.89 shows that, under the assumption of linear elastic behavior, stresses at a particular point can be expressed as a linear combination of global shape functions and generalized, nodal, coordinates.

As mentioned in [TobiasEberhard09], the derivation of the stresses for the entire finite element model and the reduced model are slightly different. For the entire model, each nodal DOF has to be loaded with a unit displacement while the remaining ones have to be set to zero. The stress distribution in the flexible body has to be calculated with the help of a finite-element solver. Usually, to reduce the information contained in the stress distribution, only stress values in nodal points are recorded. These values can be interpreted as stress mode Υ_{ei} belonging to the DOF i loaded with the unit displacement. All of these modes are assembled in a matrix

$$\boldsymbol{\Upsilon}_e = [\Upsilon_{e1}, ..., \Upsilon_{ei}, ..., \Upsilon_{eN}] \in \mathbb{R}^{2N\times N}, \tag{2.90}$$

where N is the number of DOF of the entire model. If $\boldsymbol{\sigma_e} \in \mathbb{R}^{2N\times 1}$ is a vector containing the stresses for all the $N/3$ nodes of the model,

$$\begin{aligned}\boldsymbol{\sigma}_e = [&{}^1\sigma_{11},\ {}^1\sigma_{22},\ {}^1\sigma_{33},\ ,{}^1\tau_{12},\ {}^1\tau_{13},\ {}^1\tau_{23},\\ ...,&{}^{N/3}\sigma_{11},\ {}^{N/3}\sigma_{22},\ {}^{N/3}\sigma_{33},\ ,{}^{N/3}\tau_{12},\ {}^{N/3}\tau_{13},\ {}^{N/3}\tau_{23}]^T,\end{aligned} \tag{2.91}$$

it is possible to express the stresses as

$$\boldsymbol{\sigma}_e = \boldsymbol{\Upsilon}_e \cdot \boldsymbol{q}_e. \tag{2.92}$$

In the case of stress computation for the reduced model, each column of the projection matrix can be interpreted as a displacement field of the entire finite-element model, that belongs to a configuration, where the i^{th} DOF of the reduced model is set at one and the others are set at zero. Therefore, the entire FE model can be loaded with the i^{th} column of the reduction matrix $\boldsymbol{V}$ and the resulting stress distribution, computed only in the nodes, is the stress mode $\Upsilon_{ei,red}$ belonging to the reduced DOF i, which was loaded.

By analogy it is possible to assemble a matrix $\boldsymbol{\Upsilon}_{e,red} \in \mathbb{R}^{2N \times n}$ which computes the nodal stresses as a combination of the reduced coordinates

$$\boldsymbol{\sigma}_e \approx \boldsymbol{\sigma}_{e,red} = \boldsymbol{\Upsilon}_{e,red} \cdot \boldsymbol{q}_{red} = \boldsymbol{\Upsilon}_e \cdot \boldsymbol{V} \cdot \boldsymbol{q}_{red}. \tag{2.93}$$

So a relation between the full and reduced stresses matrices is established

$$\boldsymbol{\Upsilon}_{e,red} = \boldsymbol{\Upsilon}_e \cdot \boldsymbol{V}. \tag{2.94}$$

It is possible to compute the stress matrix $\boldsymbol{\Upsilon}_{e,red}$ in *GTM* with the functions *gtm_writeAbqRedInp* and *gtm_MakeStress*. The first one creates an Abaqus job input file. Running this file will solve the stress finite element problem explained before. Once the solver is finished a .fil file will be created with all the information of the stress matrix. The second function reads the .fil file and assembles the final stress matrix.

In order to improve efficiency, not all the nodal stress distribution is computed. Stresses are only computed at the nodes of interest and those in the vicinity with the intention of providing an accurate result. That is, if stresses for a surface node is required, the stress matrix will be computed for 18 nodes. The one of interest and the other 17 nodes nearby, but only the stresses for the original node are valid.

Chapter 3

Preliminary investigations using a simple beam model

In this chapter, simulations with a simpler model than the gears are made in order to obtain the first results in a faster way. The main objective of working with the beam model is to learn about the behavior of *GTM* and the stress results delivered by the used tool chain with different types of reduction matrices. In all the simulations made, an arbitrary node, see Fig. 3.1, is loaded with a sinusoidal force. Displacements and stresses on the node are computed.

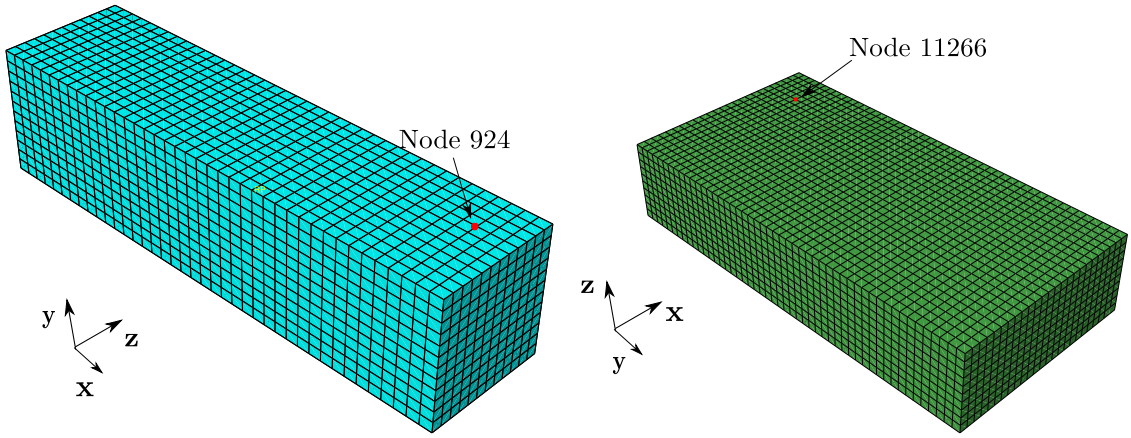

Figure 3.1: Beam models and nodes loaded used in this chapter.

The structure of this chapter is the following: First of all, the procedures followed during all simulations are explained. Then, in Section 3.1, the first beam model is introduced and its main characteristics presented. Finally, in Section 3.2, a second model is introduced see Fig. 3.1(b). In each section results from the simulations are shown and discussed.

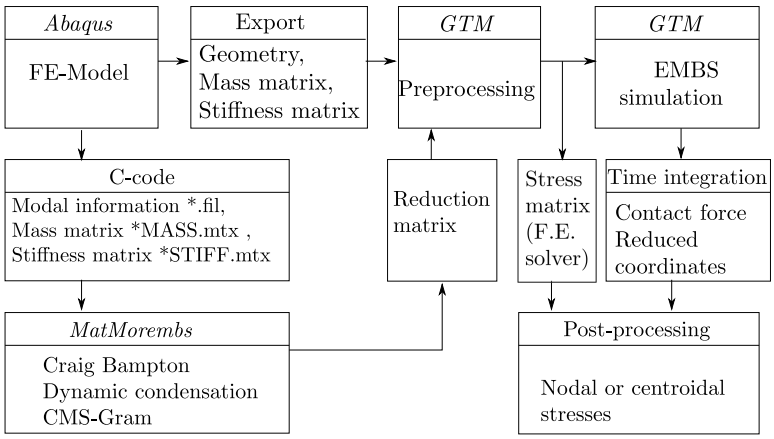

Figure 3.2: Flow diagram of all the processes.

In Fig. 3.2, the scheme adopted in order to compute the problem and reduce the matrices is presented.

First of all, a model is set up in Abaqus and solved. This model is the benchmark which is used to compare all the simulations in *GTM* against.The input file of this model is the one that will provide all the relevant information, i.e. geometry and modes, to *MatMorembs* and *GTM*.

After integration, *GTM* by default provides the position, quaternions and velocities, translational and rotational, of the reference frame. The contact forces, if contact exists, other forces and torques, like the single force used with this model, and the set of reduced coordinates are also computed. In order to recover the nodal stresses, a post-processing step is required, see Section 2.4.

3.1 Squared section beam model

The first beam model used has a squared section beam and is loaded at node 924 with a sinusoidal force of 1 kN in Y-direction, see Fig. 3.1(a). The beam has a length of 200 mm and its normal section is a 50×50 mm^2 square. The finite element model, set up in *Abaqus*, has the following characteristics: The beam is made of standard steel with a density of 7850 kg/m^3, a Young's modulus of $2.1 \cdot 10^{11}$ Pa and a Poisson's coefficient of 0.3.

The geometry is meshed with hexahedral C3D8R elements. The model has a total of 5760 elements and 6929 nodes. Each node has 3 DOFs; therefore, the free system has 20787 degrees of freedom. The bore of the beam is defined by the 69 nodes of its central section. A reference frame is attached to the center of

gravity and coupled kinetically with the bore. Consequently 507 DOF are locked during simulations.

For the EMBS model simulations performed with different reduction matrices, see Table 3.1, no stresses could be recovered. Numerical errors seem to appear during the integration on *GTM*. Those problems are attributed to symmetries on the model: Modes are symmetrical, see Fig. 3.3, and half of the beam remains static while the other half is excited.

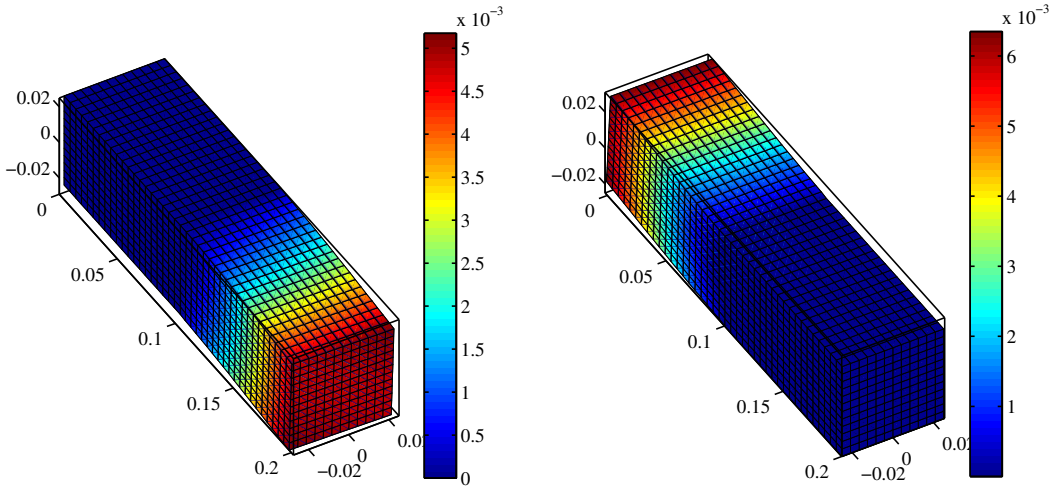

Figure 3.3: Qualitative representation of the 1^{st} and 3^{rd} flexing modes of the model.

Table 3.1: Reduction matrices used to integrate the symmetric model.

Model	Ansatz function
Model 1	100 eigenmodes.
Model 2	Craig Bampton with 100 normal modes and 3 constrained modes (at node 924).
Model 3	200 eigenmodes.
Model 4	Craig Bampton with 200 normal modes and 3 constrained modes (at node 924).

To illustrate the behavior of this beam, results from Model 1 and Model 2 are shown in Fig. 3.4. Nodal displacements and normal stresses are computed at node 924. A clue that something unusual is happening during the simulation can be observed in normal stress in the Y-direction, see Fig. 3.4(d). Eigenmodes are unable to recover local deformations and stresses. They can only image global

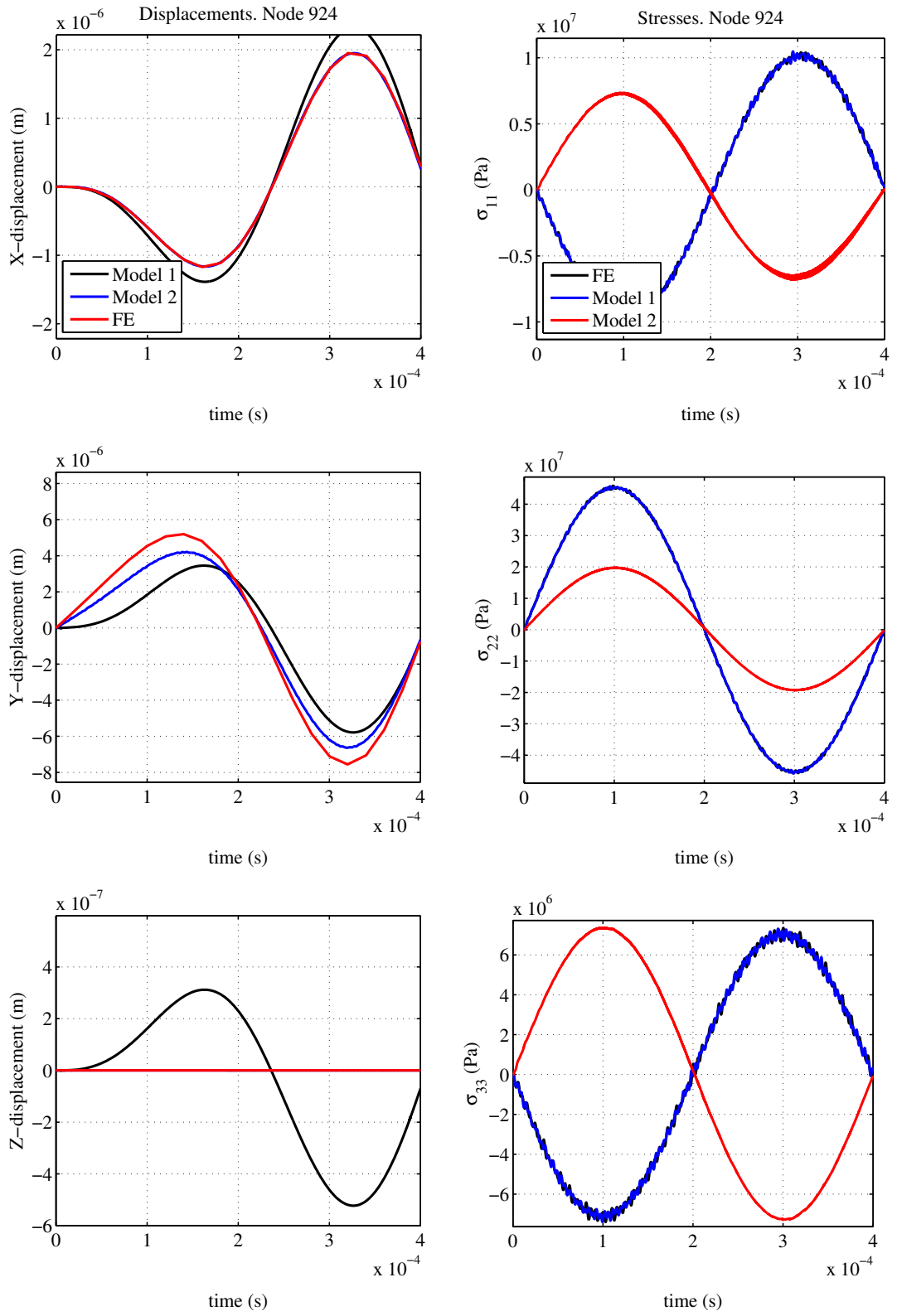

Figure 3.4: Results for Models 1 and 2 (see Table 3.1) Nodal displacements are shown on the left side. Normal stresses on the right side.

stresses. Therefore, when these kinds of matrices are used to recover stresses, the computed stress is much lower than the one obtained from the FE model. However, in this case, the opposite happens. Also, looking at the other two stress components, there is no resemblance between the stresses recovered with *GTM* and those computed with *Abaqus*.

In summary, it can be said that each four modes of the model, in theory, share the same eigenfrequency. This anomaly leads to numerical problems when the model is integrated in *GTM* and the results obtained are not reliable or representative. In consequence, another model is set up to try to bypass this situation. The new beam is bounded differently and symmetries are avoided. A more dense mesh is also used.

3.2 Rectangular section beam model

A rectangular section beam is chosen in order to perform the new simulation. Again, a sinusoidal vertical force in Z-direction has been applied at the node seen in Fig. 3.1. Simulations are done using two forces with the same amplitude of 100 N with different frequencies of 2500 Hz and 5000 Hz in order to measure the behavior of the system with different excitations. The beam dimensions are the following: in X-direction, 0.5 m; in Y-direction, 1 m and in Z-direction, 0.2 m.

The reference frame is attached at the center of the beam at point, $\boldsymbol{O} = [0,\ 0,\ 0]$. The beam is made of steel with an elastic modulus $E = 2.1 \cdot 10^{11}$ Pa, a density $\rho = 7850$ kg/m^3 and a Poisson coefficient $\nu = 0.3$.

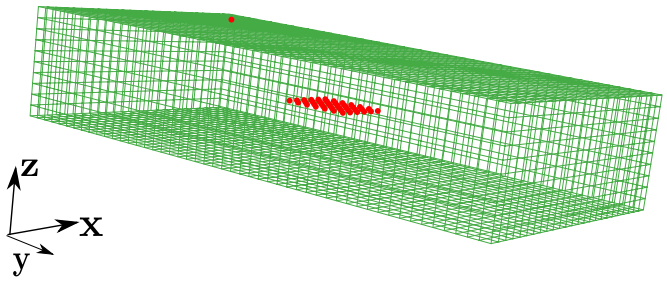

Figure 3.5: Loaded node and bore nodes. All DOF of the bore nodes are locked during the simulations.

The finite element model has been set up in *Abaqus* with the following characteristics: the mesh is made with hexahedral C3D8R elements with a total of

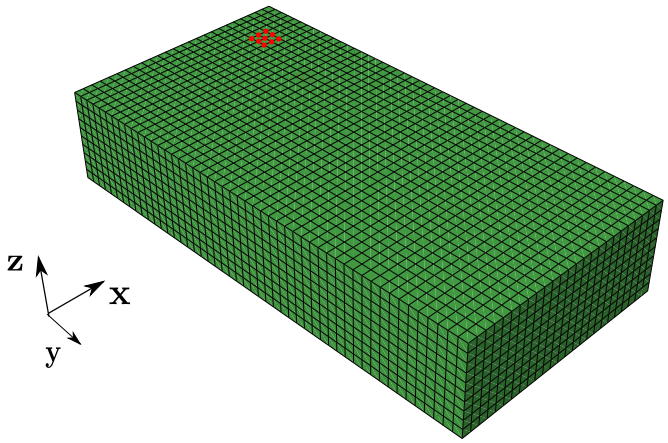

Figure 3.6: External nodes used in the Craig Bampton reduction.

14586 nodes. Each node has 3 degrees of freedom (displacements in X-, Y- and Z-directions). Accordingly, the free model has 43758 degrees of freedom.

The reference frame, attached to the model used in all the simulations, is locked. Therefore, all the bore nodes, 42 nodes, are locked as there is a kinematic coupling between these nodes and the reference frame. Consequently, in the bounded model there are 43632 degrees of freedom. The constrained mass, $\boldsymbol{M}_e$ and stiffness $\boldsymbol{K}_e$, matrices are of size (43623×43623). The force is acting on node 11266 in the negative Z-direction, as seen in Fig. 3.1(a).

Table 3.2 summarizes the different assembled models. Model 5 is assembled with the first 100 eigenmodes. The first eigenfrequency is 298.5 Hz, the 100^{th} is 11230 Hz. For the Craig Bampton reduction matrices node 11266, in the case of Model 6 and Model 8 is chosen as external node. Node 11266 and the eight

Table 3.2: Reduction matrices used to integrate the symmetric model.

Model	Ansatz function
Model 5	100 eigenmodes.
Model 6	Craig Bampton with 10 normal modes and 3 constrained modes.
Model 7	Craig Bampton with 50 normal modes and 27 constrained modes.
Model 8	Craig Bampton with 100 normal modes and 3 constrained modes.
Model 9	Craig Bampton with 100 normal modes and 27 constrained modes.
Model 10	Dynamic condensation with 50 normal modes and 3 dynamic modes.
Model 11	Gram reduction with 50 modes.

nodes surrounding it, see Fig. 3.6, are set as boundary nodes in Model 7 and 9.

For Model 10, the condensation frequency is 5000 Hz, and finally, the CMS-Gram Matrix of Model 11 is assembled with node 11266 set as interface node. The condensation frequency is set as 0 Hz, i.e. Craig Bampton constrained modes are computed. The frequency range for the gramian matrices computation is set to be $[0; 6000]$ Hz. Finally, for the intermediate Krylov reduction 6 equally spaced shifting points, [0 to 6000] Hz, are chosen. Six moments are matched at each shifting point.

3.2.1 Simulation results and discussion

As one of the objectives of this work is to find a set of reduction modes which allow efficient computation, it is interesting to note how much time the FE solver needs in comparison with *GTM*. A summary of the integration results with both frequencies is presented in the following table (Table 3.3):

Table 3.3: Integration times for the FE solver and the different *GTM* reduction matrices.

Model	Alias	frequency: 2500 Hz	frequency: 5000 Hz
FE model	FE	2.003 min	2.020 min
Model 5	EM (100)	0.354 min	0.441 min
Model 6	CB (3&10)	1.3296 min	1.723 min
Model 7	CB (27&50)	2.100 min	2.340 min
Model 8	CB (3&100)	1.705 min	1.990 min
Model 9	CB (27&100)	2.324 min	2.071 min
Model 10	DC (3&50)	1.2016 min	1.4477 min
Model 11	CMS-G (50)	1.5508 min	1.756 min

It can be observed that, as expected, all except two reduction methods employ less time to complete the integration than the FE solver. Using only eigenmodes it is possible to save between 94 and 99 seconds approximately in each simulation. However, as simulations have shown, using only eigenmodes it is feasible to model correctly the contact force and the kinematics of the gear but, unless an impractical number of eigenmodes is used, it seems impossible to investigate the stress recovery, see Fig. 3.7.

The reason is that eigenmodes are able to image global deformations and, therefore, stresses very well but not local deformations and stresses. Nevertheless, computational time is also saved with other reduction matrices: as many as 48 seconds, a 39.94 %, can be saved if a dynamic condensation is used. Although it

may not seem very much, if 48 seconds can be saved working with a very simple model, greater and meaningful savings can be expected when researching with more complex models.

In the following figures, Fig. 3.7 and Fig. 3.8, it is possible to observe the quality of the stresses computed with GTM for the two forces with different frequencies. To avoid redundancies only the normal stresses in X-direction, σ_{11} and in Z-direction, σ_{33} are shown. The conclusions obtained with this stress can be used for the other normal stress σ_{22}, but not for the shear stresses:

Unlike nodal displacements, which are computed directly at the nodes, *Abaqus* computes strains and stresses at the Gauss integration points which depend on the used element type. Subsequently, these values are extrapolated to the nodes if nodal stress is computed. Throughout this process, shear stresses are not correctly obtained and are not reliable.

On the other hand, if centroidal stress is computed, *Abaqus* proceeds in a slightly different way. In this case only one Gauss integration point is used per element. This point coincides with the centroid of the element, so the strains and stresses can be directly computed and no extrapolation is needed. As a consequence, all the stresses computed in this way are reliable.

More research needs to be done in order to establish the exact differences between the computation of nodal and centroidal stresses and why only unreliable results are obtained with shear stresses. In this thesis, it is accepted that for nodal stresses, shear components are not properly computed in *Abaqus* and, therefore, are not displayed in the results.

Looking at the results obtained, it is possible to extract some general conclusions. In all the cases computed, a high frequency component appears which is not present in the FE result. In the case of the stresses computed with GTM, almost no material damping is included ($\beta_R = 1^{-12}$). However the integrator scheme of the FE solver is able to smooth these oscillations. Nevertheless, all the reduction techniques shown can follow the stress curves provided by the finite element software.

No more research on this topic has been done in this thesis, but it would be interesting to investigate how, despite introducing no numerical damping, the FE integration scheme solves the problem avoiding the high frequency oscillations that appear in the same setup when GTM is used.

In order to determine which reduction type delivers most accuracy, an error estimation is performed. If $\boldsymbol{\sigma}_{ii}^{GTM}$ and $\boldsymbol{\sigma}_{ii}^{FE}$ are vectors which store the normal stresses of each time step in X-, Y-, and Z-directions computed with GTM and the FE solver respectively. Then, if there are m time steps, the error is calculated

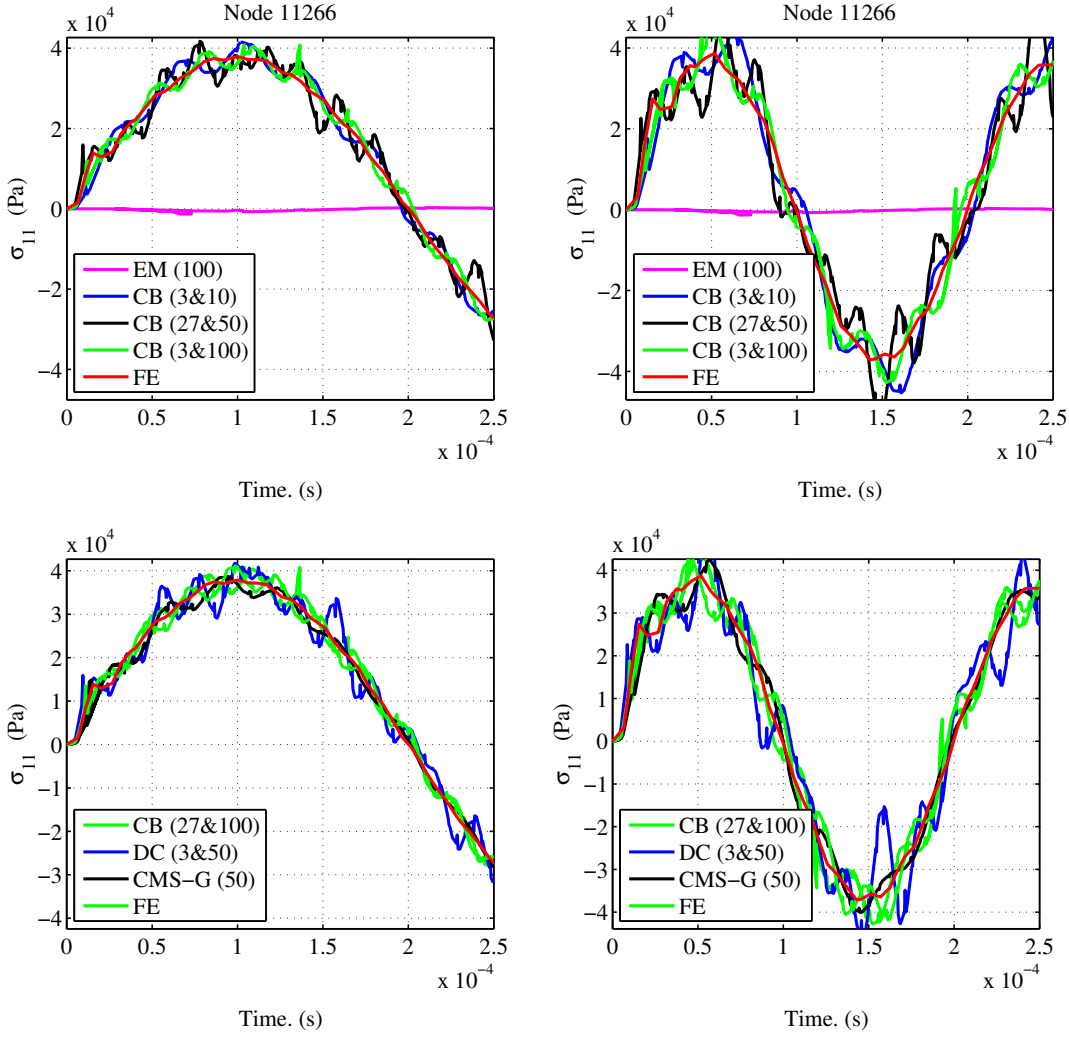

Figure 3.7: On the left results for the normal stress in X-direction are displayed for a frequency of 2500 Hz. On the right, force amplitude is maintained, but the frequency is doubled.

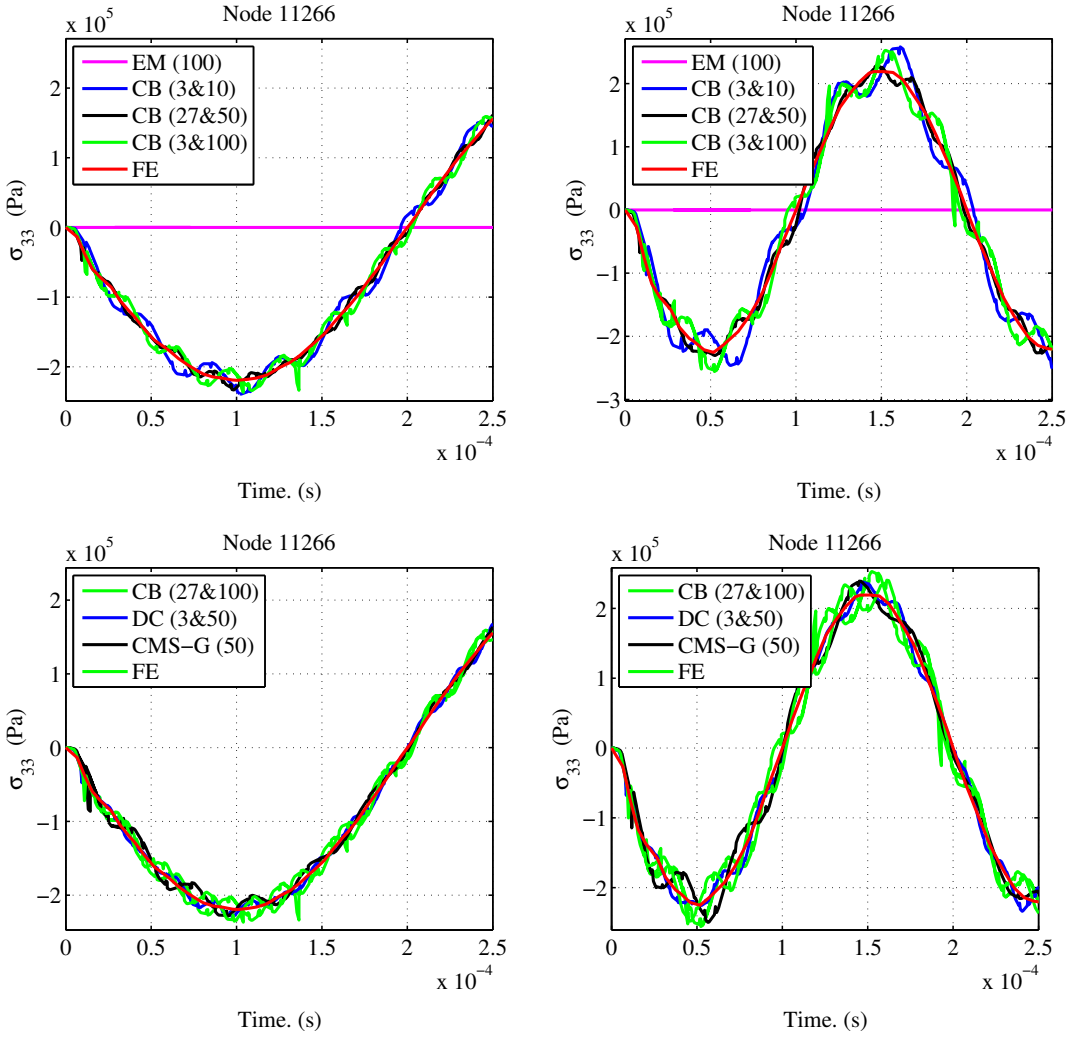

Figure 3.8: Normal stresses on Z-direction. On the left, those obtained for a force frequency of 2500 Hz. On the right, the force frequency is 5000 Hz.

as

$$E_{ii} = \frac{\sum_{k=1}^{m} \left(|\sigma_{ii,\,m}^{FE} - \sigma_{ii,m}^{GTM}| \right)}{m}, \qquad E = \frac{\sum_{ii=1}^{3} E_{ii}}{3}. \tag{3.1}$$

In Fig. 3.9 and Fig. 3.10, it is possible to observe that the dynamic condensation and the CMS-Gram method seem to have the greatest potential. With a smaller number of modes the results are better than those obtained with the two Craig Bampton reduction matrices. However, the main drawback of the CMS-Gram method is the noticeably greater computational effort required to assemble the reduction matrix in comparison with the Craig Bampton method: despite being twice as big, the Craig Bampton matrix is assembled in less time than the CMS-Gram reduction matrix. This is the main reason for continuing to use Craig Bampton matrices in the following steps of this work.

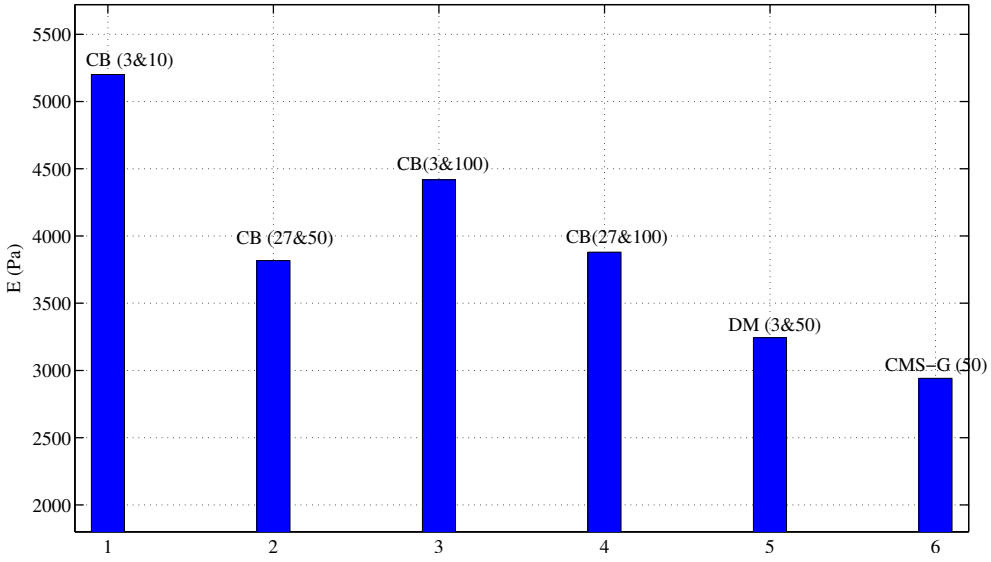

Figure 3.9: Error estimation for a force frequency of 2500 Hz

Focusing on the Craig Bampton method, it can be seen that those matrices with 9 nodes being set as constrained modes seem to recover stresses better than those with only three constrained modes. Also, the higher the number of eigenmodes, the better the results are, but only up to a certain limit. During the simulations, it was observed that the larger the number of constrained modes, a larger number of eigenmodes is needed to produce good results. But once this criterion is reached, increasing the number of eigenmodes does not bring any further benefit, as it can be seen with Model 7 and 9. However, it is true that

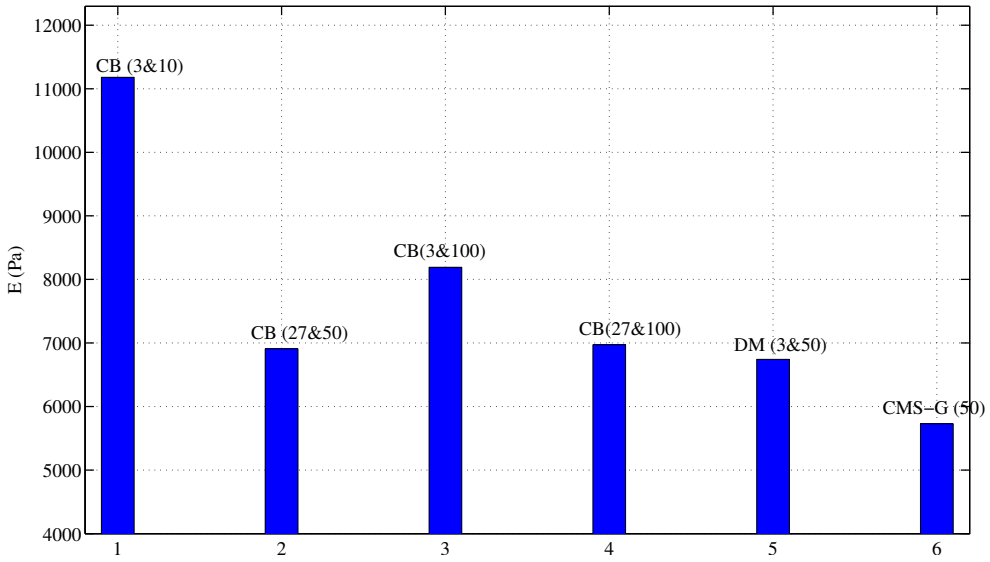

Figure 3.10: Error estimation for a force frequency of 5000 Hz

with larger numbers of eigenmodes, the oscillations observed are smaller, which leads to shorter integration times (as seen in Fig. 3.10 with Models 7 and 9).

Dynamic condensation, Model 10, provides good results because in this case the interaction force is well-known since it is a defined parameter. Presumably, the best results should be provided when the force frequency is the same as the condensation frequency, but this case it is difficult to judge. Errors are significantly larger when the 5000 Hz force is applied, so a direct comparison is not valid. If Model 2, which is by far the worse in both cases, is taken as a reference and a relative error is computed as

$$E_r = \frac{E_{10}}{E_2}. \tag{3.2}$$

Then,

$$E_{r,2500} = 0.6236 \quad \text{and} \quad E_{r,5000} = 0.6030.$$

From Eq. (3.2), it is possible to see that when the force frequency matches the condensation frequency, the dynamic condensation provides a slightly better result. Nevertheless, when the interaction is unknown it is difficult to establish the space of frequencies in which to perform the dynamic condensations. If a very large range is used, it will also become computationally expensive.

Chapter 4

Stress recovery in gear simulations

Because it was possible to compute local deformations and stresses in the beam model, more complex models can be tested. Before beginning simulations with two gears, a preliminary investigation has been performed with one gear and a single load in order to verify that the results obtained with the beam can be carried over to a bigger and more complex model. After results are confirmed, the final model with two gears in contact is assembled and studied.

4.1 *Ritzel* loaded with a single force

The gear used in this preliminary step is a pinion gear called *Ritzel*. It has 18 teeth and is made of standard steel. This steel has Young's modulus $E = 2.1 \cdot 10^{11}$ Pa, Poisson ratio $\nu = 0.3$ and density $\rho = 7850$ kg/m^3 The finite-element model characteristics are as follows:

The gear is modeled with 103419 nodes and 86064 elements. These elements have hexahedral geometry and are of C3D8R type. Each node has 3 degrees of freedom active, that are three displacements in X-, Y- and Z-directions. So the free model has 310257 active DOF. The 960 nodes that form the bore are kinematically coupled with a reference frame whose origin coincides with the center of gravity of the gear. In these simulations, the reference frame is locked, so no rotational or translational movement is permitted. Therefore the constrained model is bonded by 2880 DOFs to the surrounding environment and 307377 remain active.

The force is acting at node 27788,which is located on one flank, see Fig. 4.1, on

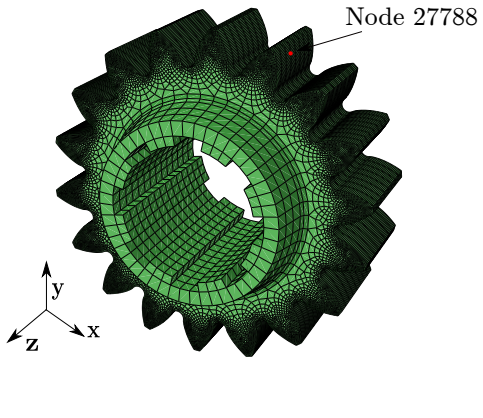

Figure 4.1: Ritzel and node loaded with the sinusoidal force.

the negative X-direction. It is again an harmonic force function given by:

$$F_x = -100sin(2\pi 2500t) \text{ N}. \tag{4.1}$$

Five reduced models, see Table 4.1, have been tried with this gear. The constrained modes for Model 2 and 3 are computed at the node 27788. Constrained modes for Model 4 are computed at the loaded node and the eight surrounding nodes. To assemble the CMS-Gram reduction matrix, node 27788 is set as interface node. The frequency range in which the Gramian matrices are computed is from 0 to 6000 Hz. Six matching points are defined in this range and at each point, 6 moments are matched in the intermediate Krylov reduction.

In order to compare the computational efficiency of *GTM* and the FE solver, all

Table 4.1: Reduced models used in the simulation.

Model	Alias	Ansatz function
Model 1	EM (300)	300 eigenmodes.
Model 2	CB (3&61)	Craig Bampton reduction with 61 normal modes and 3 constrained modes.
Model 3	CB (3&300)	Craig Bampton reduction with 300 normal modes and 3 constrained modes.
Model 4	CB (27&300)	Craig Bampton reduction with 300 normal modes and 27 constrained modes.
Model 5	CMS-G (64)	CMS-Gram reduction.

the integration times are summarized in Table 4.2. The three normal stresses at node 27788 have been computed and are displayed in Fig. 4.2.

Looking at the results of Figs. 4.2(a), 4.2(b) and 4.2(c), is possible to observe that a very high frequency component, that does not exist in the FE solution, appears when the integration is done with *GTM*. This can be associated with instabilities during the integration as no significant material damping is included. These instabilities are more significant when the system is reduced with the CMS-Gram technique, hence the higher computational time shown in Table 4.2.

As mentioned with the beam model, the difference related to the high frequency noise observed in *GTM* is that the FE solver somehow damps out the system, making it more stable than the one integrated with *GTM*.

Nevertheless, for the other two stress components, σ_{11} and σ_{33}, the CMS-Gram reduction matrix seems to fit better than the stresses computed with the Craig Bampton reductions.

If an error estimator is worked out from the data in Eq. (3.1) and is plotted, Fig. 4.3 shows the result. As Fig. 4.3 illustrates, when comparing the two methods globally, the CMS-Gram reduction technique error estimator has a lower value than the one using data from a Craig Bampton reductions.

In Fig. 4.2(d), a comparison between Model 3 and Model 4 is done. Both models have the same number of eigenmodes but differ in the constrained modes: while Model 3 has only three constrained modes computed at the loaded node,the node 27788 of Model 4 and the eight surrounding nodes are set as external nodes. Different behavior can be obtained between both models: the high frequency component is more intense in Model 4. Also, the error, see Fig. 4.3, is noticeably larger when Model 4 is used. Results get worse when nodes with no interaction are set as external nodes in the Craig Bampton method. These oscillations have an effect on the integration time, which increases significantly due to a smaller integration step.

Nevertheless, with these tests performed it is possible to state that it is still pos-

Table 4.2: Integration times for the FE solver and the different *GTM* reduction matrices.

Model	time	Model	time
FE model	22.100 min	Model 3	4.8236 min
Model 1	0.6228 min	Model 4	92.1461 min
Model 2	2.045 min	Model 5	13.786 min

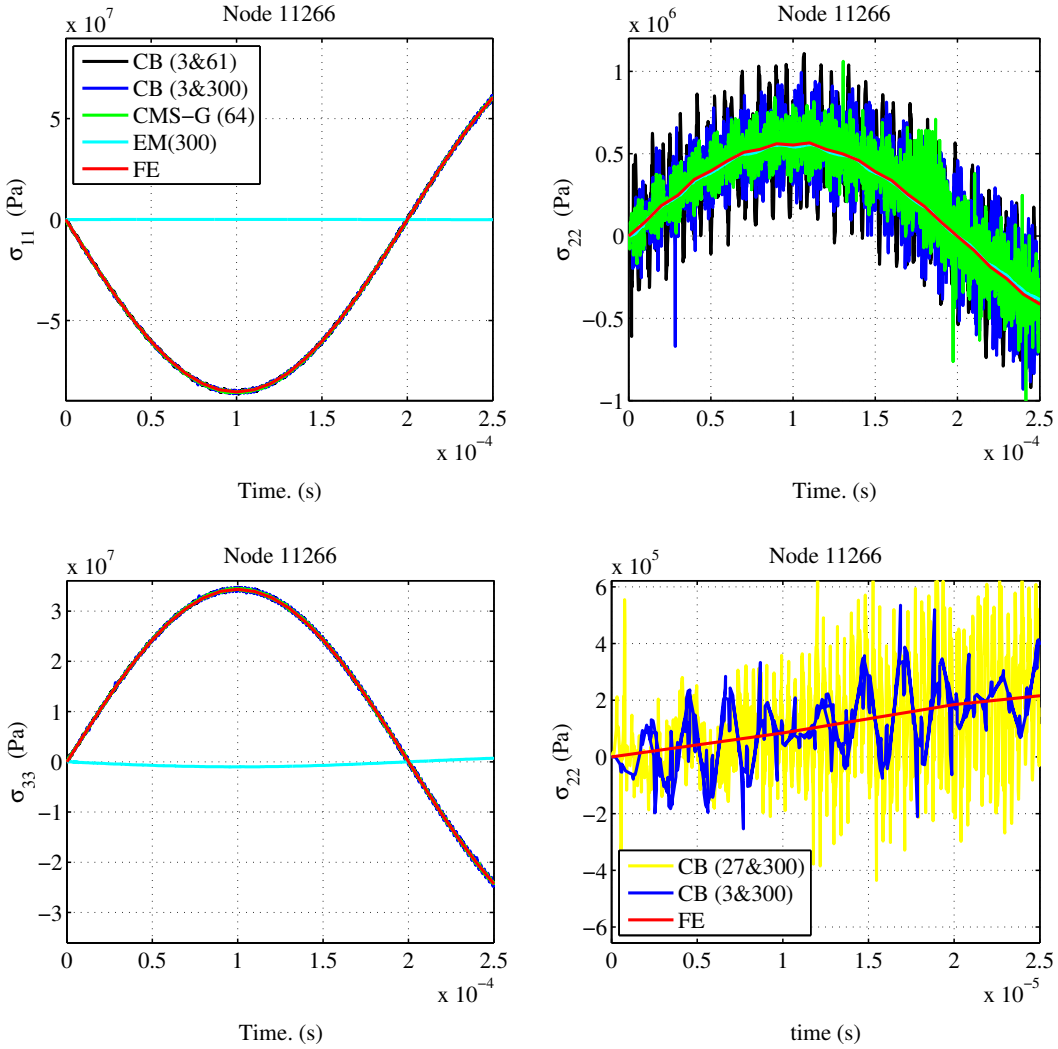

Figure 4.2: Normal stresses are computed with four reduction matrices. Fig. 4.2(a) shows stresses in the X-direction. Fig. 4.2(b) represents the normal stresses in Y-direction. Figure 4.2(c) displays the stresses in Z-direction. Finally, Fig. 4.2(d) presents a comparison of the stress in Y-direction between Model 3 and Model 4.

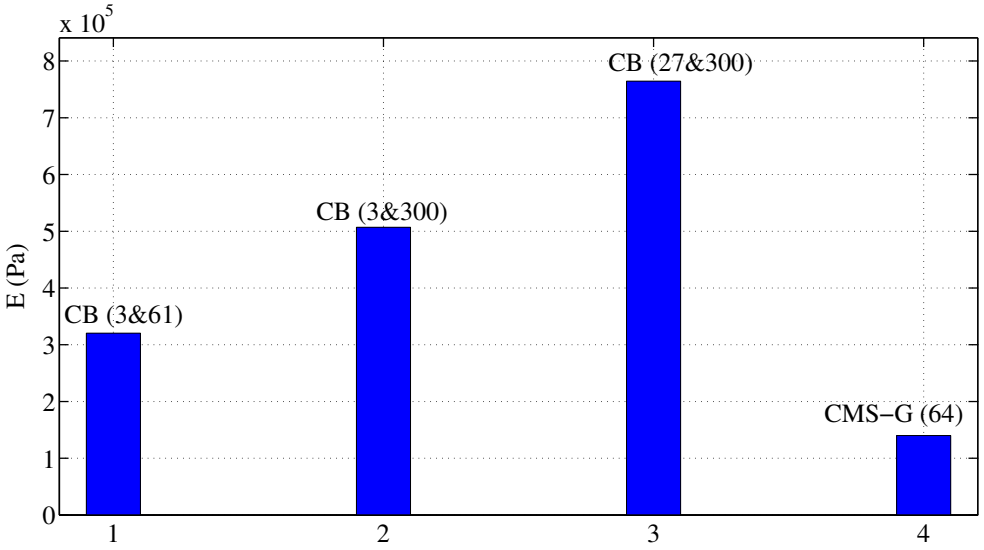

Figure 4.3: Error estimation for the two reduction techniques.

sible to recover the local stresses in a more complex model and with significantly more degrees of freedom than the beam. So, when working with a gear pair, if the contact force is modeled correctly, these types of reduction matrices should make it possible to recover the stresses of the flank of the contact teeth.

4.2 *Ritzel* and *Grossrad* system

Finally, in this section the model is assembled with two gears that are in contact. As the *Ritzel* is the same gear as used in Section. 4.1, only the characteristics of the finite-element model of the *Grossrad* are presented. The *Grossrad* is also made of the same steel as the *Ritzel*, so its density is $\rho = 7850$ kg/m^3, its Poisson's ratio $\nu = 0.3$ and its Young's modulus $E = 2.1 \cdot 10^{11}$ Pa.

The discretized model of the *Grossrad* has 208270 nodes and 173696 hexahedral C3D8R elements. Each node has associated 3 degrees of freedom, so the whole free model has a total of 624810 DOFs. A reference frame is attached to the center O, of the gear and is kinematically coupled with the 704 nodes that conform the bore of the gear. Both reference frames, the one attached to the *Ritzel* and the one attached to the *Grossrad*, are allowed to rotate in Z-direction, but are locked with respect to the remaining five degrees of freedom.

As all the bore nodes are coupled with the reference frame, they behave as a rigid body, they rotate only with the reference frame but no relative deformation between them is allowed. Therefore, when any type of mode is computed, the

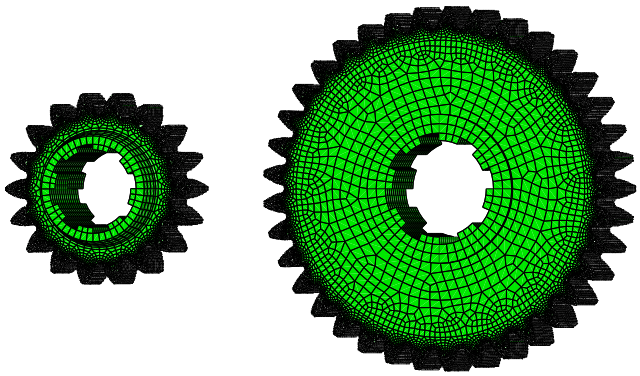

Figure 4.4: Gears used in contact research. *Ritzel* on the left and *Grossrad* on the right.

system is indeed locked. Consequently, the constrained model of the *Grossrad* has 622698 of 624810 degrees of freedom active.

4.2.1 Model setup

First of all, the model needs to be assembled in a way that the gears engage correctly. The main condition for two spur gears, i and j, to engage is that both have the same module and should engage with a distance between the centers equal to

$$D_{OO'} = \frac{(\phi_i + \phi_j)}{2} \tag{4.2}$$

where O and O' are the centers of the gears and ϕ_i and ϕ_j are the pitch diameters of both gears respectively. The data provided for these gears are the number of teeth z and the tip diameter Φ_o. The first gear, the *Ritzel*, has 18 teeth and 100 mm of tip diameter. The second gear, the *Grossrad*, is a gear with 37 teeth and its tip diameter measures 195 mm. With these numbers it is possible to compute the module, m, of a gear as

$$m = \frac{\Phi_o}{z + 2} \tag{4.3}$$

Thus, the *Ritzel*'s module is $m_r = 4.9$ mm and the *Grossrad* has $m_g = 4.9$ mm. The pitch diameter is by definition:

$$\phi = mz \tag{4.4}$$

and in consequence, $\phi_r = 88.2$ mm, $\phi_g = 181.3$ mm. With Eq. (4.2), the distance between the gear centers should be $D_{OO'} = 134.75$ mm.

Once the distance between the centers is computed, the relative rotation between the gears is left to be determined. It is important to set this angle in a way that the contact is produced in the shortest space of time, in order to reduce computational time, but avoiding penetration. After the relative position of the gears has been set, the contact penalty factor c_p needs to be established. This penalty factor is selected by the user and it should be noted that each c_p is only valid for a specific set of modes. In this thesis, the c_p parameter is selected in such a way that the contact force from the EMBS simulation matches the one provided by the FE solver.This process is summarized in Fig. 4.5.

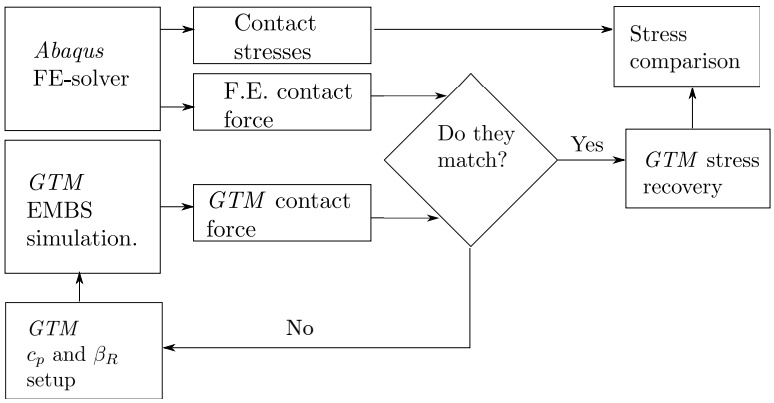

Figure 4.5: Block diagram of the penalty factor adjustment process.

Figure 4.6 shows the simulation results for a model assembled with 300 eigenmodes for each gear. The different forces and kinematics, labeled each with the number of eigenmodes used for simulation, are the result of using different penalty factors. In Fig. 4.6(a), it is possible to observe that an optimum penalty factor exists in order to match the contact force. As explained in Section 2.3.2, low penalty factors result in inaccurate enforcement of the contact constraints and therefore the contact force and kinematics do not match.

On the other hand, excessively large values result in an ill-conditioned modified stiffness matrix, see Eq. (2.65), and numerical instabilities appear. These instabilities are reflected as larger oscillations in the nodal coordinates, see Fig. 4.6(b) and Fig. 4.6(c), and consequently oscillations in the contact force.

It is also observed that, when reduction matrices are assembled with constrained modes, larger penalty factors should be used. Constrained modes have much larger associated pseudo-eigenfrequencies than the original eigenfrequencies. Hence, numerical errors described in Section 2.3.2 are less critical and it is possible to use a larger penalty factor.

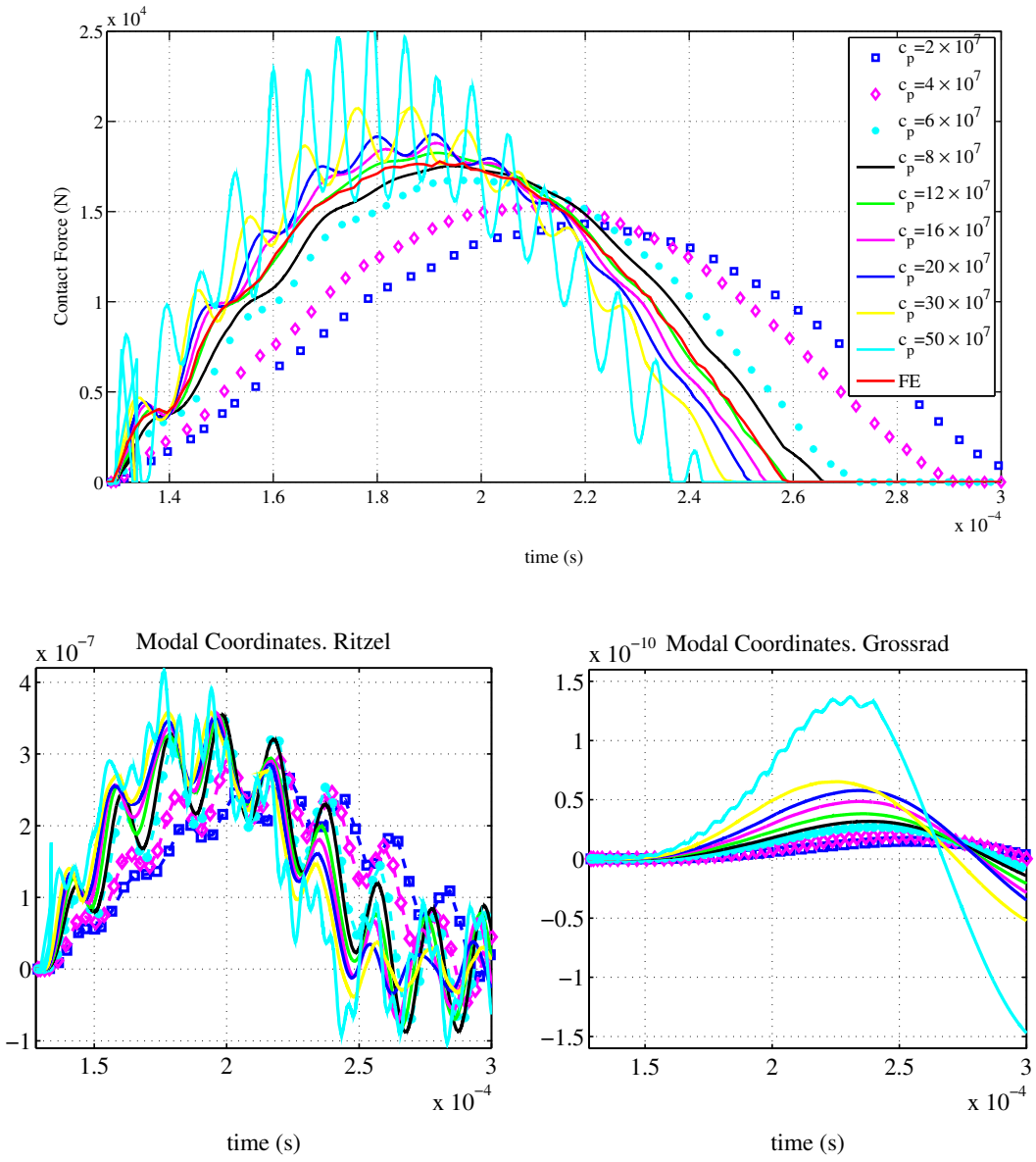

Figure 4.6: Contact force and first modal coordinate for different penalty factors.

4.2.2 Simulation results and discussion

Once the model is setup, a preliminary step is needed in order to compute the reduction matrices. As seen in Section 4.1, when the reduction matrix is computed with nodes with no interaction set as external nodes, greater instabilities appear. So, knowing the contact nodes, i.e., the nodes at which a contact force appears during the simulation, becomes critical to assemble the Craig Bampton or CMS-Gram reduction matrices.

To do this, a reduction matrix is assembled with the first 300 eigenmodes and a simulation in *GTM* is performed. When completed, the contact nodes are extracted and other reduction matrices, summarized in Table 4.3, can be constructed.

Table 4.3: Reduced models and their abbreviation used in the simulation.

Model	Alias	Ansatz function
Model 1	EM(300)	300 eigenmodes.
Model 2	EM(600)	600 eigenmodes.
Model 3	FE-M	50 eigenmodes and the nodal deformation pattern from *Abaqus*.
Model 4	CB(81&300) CB(108&300)	Craig Bampton reduction with 300 eigenmodes and 81 normal modes(*Ritzel*) or 108 constrained modes (*Grossrad*).
Model 5	DC(81&300) DC(108&300)	Dynamic condensation. 300 normal modes and 81 or 108 constrained modes.
Model 6	CMS-G(162) CMS-G(213)	GMS-Gram reduction with 162 (*Ritzel)* modes and 123 modes (*Grossrad*).
Model 7	CMS-G(381) CMS-G(408)	CMS-Gram reduction with 381 (*Ritzel*) and 408 modes (*Grossrad*).

For the Craig Bampton method, the dynamic condensation and the CMS-Gram methods, Models 4, 5, 6 and 7, the contact nodes are set as external nodes. In Model 5, the condensation frequency based on the duration of the contact force has been set as 5 kHz. The Gramian matrices for Models 6 and 7 have been computed with a range of frequencies from 0 to 6 kHz. For Model 6, two shifting points are defined and two moments are matched at each one. For Model 7, three shifting points with 3 matching moments each are defined.

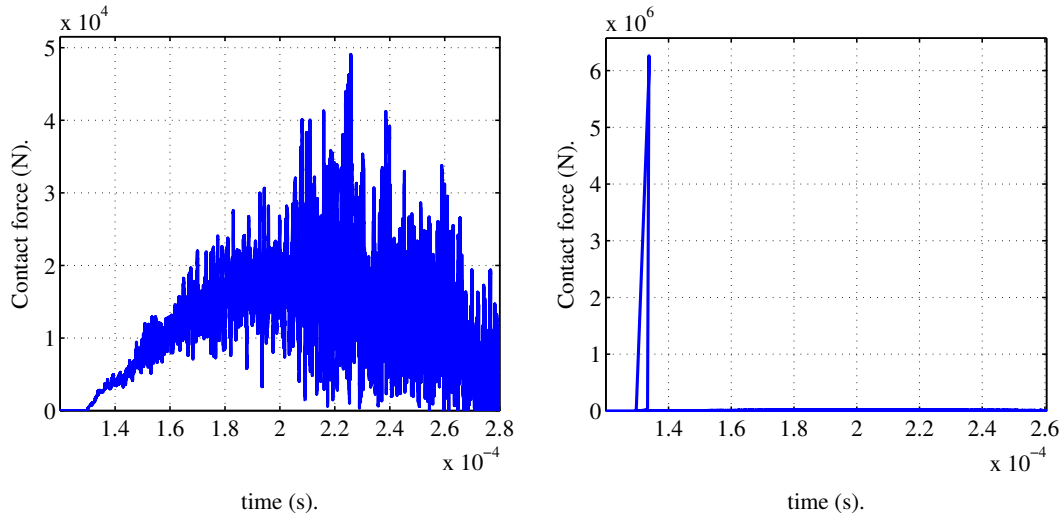

Figure 4.7: Contact forces computed with no damping and constrained modes in the reduction matrices.

The first set of simulations is done without introducing damping in the elastic formulation, as the default β-Rayleigh, $\beta_R = 10^{-12}$, is close to zero. Even though when only eigenmodes are used no problems appear, the inherent stiffness of the constrained modes causes the appearance of high frequency oscillations in the contact force, see Fig. 4.7(a). In this case, oscillations have a much higher frequency and higher amplitudes than the ones observed for the beam or the *Ritzel* with only one node loaded, and the stresses cannot be recovered in a meaningful way to be compared against the FE simulation.

However, in an attempt to bring the setup more in line with the previous models, the reduction matrix of one gear is assembled with constrained modes of the contact area. On the other hand, for the other gear there are no constrained modes computed for the contact nodes. The idea is to reduce the high frequency oscillations in the set of reduced coordinates, abandoning the possibility of recovering the stresses of one gear, where no local deformations are measured.

Several reduction matrices for the second gear, combinations of constrained modes and eigenmodes, are tried. These simulations show no improvement or very little improvement. In fact, if the second gear is reduced with only eigenmodes, the contact force, see Fig. 4.7(b), is even less representative than when the second gear is reduced with a Craig Bampton or a CMS-Gram method.

Model 3 represents another attempt to avoid oscillations. This model is assembled in a completely different way. The deformation pattern of the whole gear is taken from the FE software when the force is at its maximum. This pattern is considered as a new shape function and is combined with 50 eigenmodes to

assemble the reduction matrix. In the results, Fig. 4.8, it is possible to observe that the oscillations have been considerably reduced. Nevertheless, the practical utility of this type of reduction is very limited, as the FE model needs to be solved first. Hence, the system should be damped in order to recover stresses with more usual techniques.

In order to damp these oscillations, the β-Rayleigh is increased from 10^{-12} to $3.9 \cdot 10^{-7}$ and a new penalty factor is set accordingly. It is worth mentioning that setting the right β_R is not straightforward. There is an optimum value of the damping parameter: with lower values, oscillations on the contact force are still very noticeable, and, higher values generate the appearance of new oscillations and significantly increases (at least in one order of magnitude) the integration time. Therefore, the value $\beta_R = 3.9 \cdot 10^{-7}$ is set by trial and error after simulating with a range of β_R between 10^{-12} and 10^{-8}.

Nevertheless, this new damping parameter is enough to get rid of the oscillations and makes it possible to perform some comparison between the different reduction matrices. The following table (4.4) summarizes the computational efficiency of all the approaches used for an integration time of 0.3 ms. It is possible to see the noticeable increase in computational time due to the increase of the β Rayleigh, even when it is at its optimum value.

Table 4.4: Integration times for the FE solver and the different *GTM* reduction matrices.

Model	time
FE model. ($\beta_R = 10^{-12}$)	48.567 min
Model 1. ($\beta_R = 10^{-12}$)	16.188 s
Model 2. ($\beta_R = 10^{-12}$)	30.768 s
Model 3. ($\beta_R = 10^{-12}$)	16.446 s
Model 4. ($\beta_R = 3.9 \cdot 10^{-7}$)	55.638 min
Model 5. ($\beta_R = 3.9 \cdot 10^{-7}$)	51.755 min
Model 6. ($\beta_R = 3.9 \cdot 10^{-7}$)	40.121 min
Model 7. ($\beta_R = 3.9 \cdot 10^{-7}$)	116.154 min

As centroidal stresses are computed this time, the problem with shear stresses, that appear when nodal stresses are computed, do not exist anymore and the results for all the stresses obtained are reliable. Hence, with the aim of condensing the information, an equivalent stress can be computed. In this case, the von Mises stress has been chosen to make the comparisons. This stress is defined as:

$$\sigma_{VM} = \sqrt{\sigma_{11}^2 + \sigma_{22}^2 + \sigma_{33}^2 - (\sigma_{11}\sigma_{22} + \sigma_{11}\sigma_{33} + \sigma_{22}\sigma_{33}) + 3(\tau_{12}^2 + \tau_{13}^2 + \tau_{23}^2)}. \tag{4.5}$$

The following graphs, Fig. 4.8, presents the computed Von Mises stresses for both gears. Stresses are computed on elements 47823 and 47828 in the case of the *Ritzel*, and on elements 5704 and 12363 for the *Grossrad*. Elements 47823 and 5704 are located in the respective contact area. Elements 47828 and 12363 are located at the dedendum of the respective teeth. Stresses obtained with the FE solver are compared with those recovered with *GTM* for all the different reduction matrices.

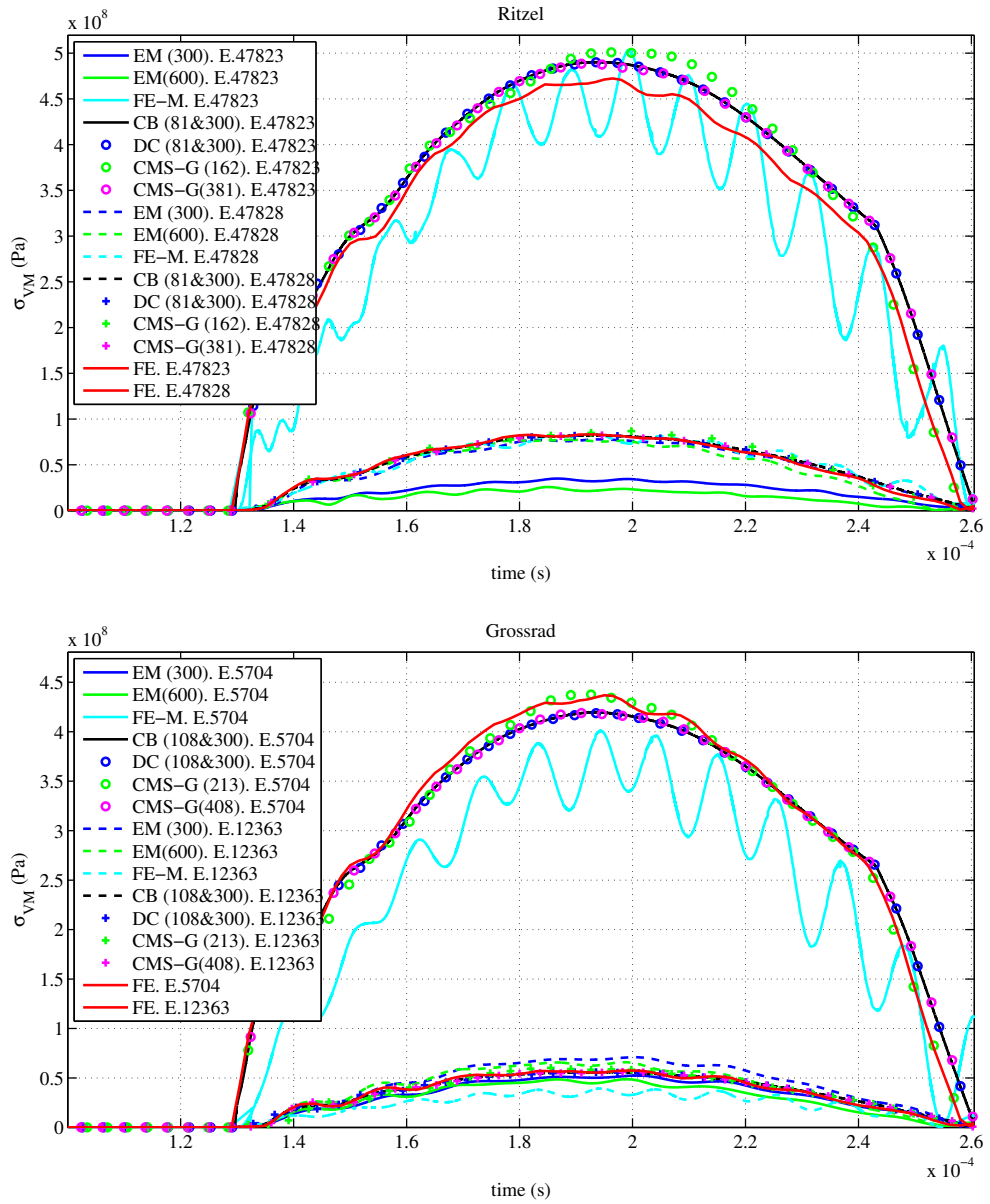

Figure 4.8: Von Misses stress comparisons. Continuous lines refer to contact stresses. Slashed lines refer to dedendum stresses.

In Fig. 4.8 it is observed that, if only eigenmodes are used, only dedendum stresses can be recovered. However, for the other reduction matrices, stresses in the contact area can also be recovered.

In order to establish which reduction technique deliver the best stress result, an error estimator is defined in a similar way as in Chapter 3: If $\sigma^{GTM}_{VM,\,i}$ and $\sigma^{FE}_{VM,\,i}$ are the values of the Von Mises stress for each i of the m-GTM integration step, the error estimator is defined as

$$E = \frac{\sum_{i=1}^{m} \left(|\sigma^{FE}_{VM,\,i} - \sigma^{GTM}_{VM,\,i}|\right)}{m}. \tag{4.6}$$

This estimator is calculated and plotted for all the reduced models.

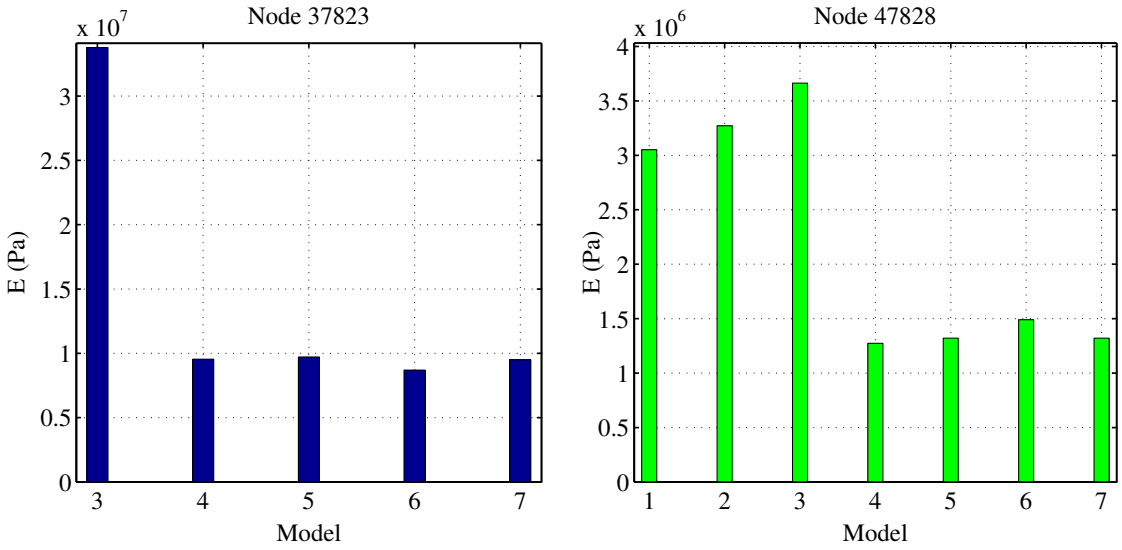

Figure 4.9: Comparison of error estimator for the *Ritzel*. Blue line represents the contact stresses. The green one, represents the dedendum stresess.

In Fig. 4.9 and Fig. 4.10, it is possible to observe the error for the dedendum stresses (green) and the contact stresses (blue) for both gears. It should be noticed that the matrices assembled as a combination of eigenmodes and other modes provide the best results in both, dedendum and contact stresses. Focusing on these matrices, in the case of Model 6, the reduced number of modes, in comparison with the 300 eigenmodes, results in a worse image of global deformations and therefore global stresses.

As expected, the CMS-Gram models provide the best results, followed by the dynamic condensation and the Craig Bampton model. It is possible to see that assembling a CMS-Gram reduction matrix with more modes does not provide a tangible improvement.

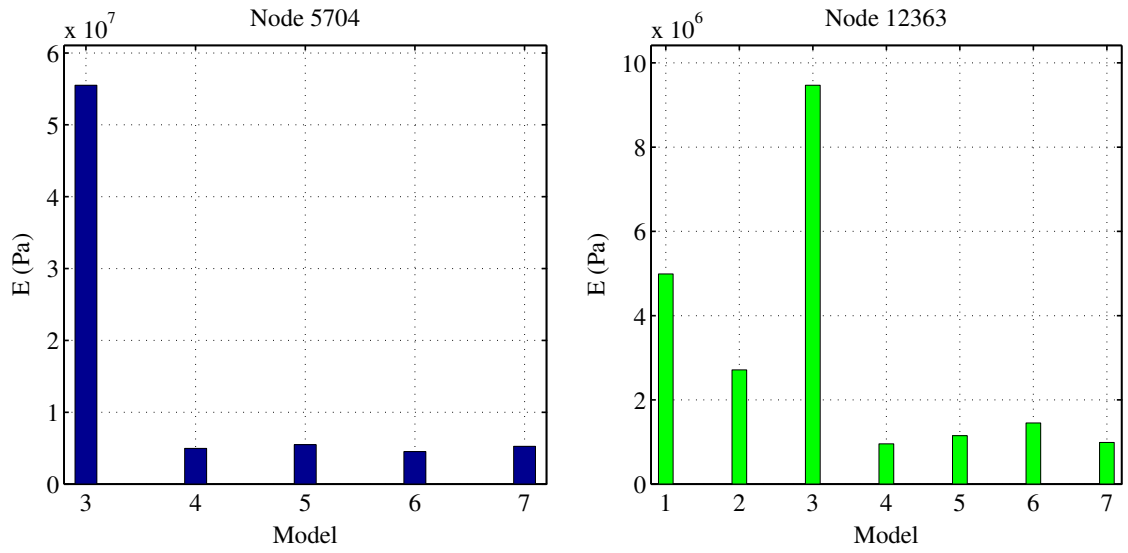

Figure 4.10: Comparison of error estimator for the *Grossrad*. Blue line represents the contact stresses. The green one, represents the dedendum stresess.

The extra modes computed in Model 7 do not contribute so much recovering the contact stress, but improves a little the dedendum stress recovery. In the end, it should also be noted that the CMS-Gram reduction matrix from Model 6 provides the best result both in accuracy and time efficiency.

Chapter 5

Conclusions

Before finishing this work, the results are analyzed and some conclusions must be extracted. Firstly, an assessment of the results obtained is carried out by comparing them with the objectives established at the outset of the thesis. Afterwards, the most troublesome aspects in the development of the thesis are highlighted with the aim of improving them in future works.

The main objective of the thesis is to validate EMBS simulations as an alternative, and computationally cheaper, way of stress recovery compared to the classical finite-element formulations, in particular, stresses as a result of gear contact. During the development of the work, it has been proved that, choosing the reduction matrices correctly, it is possible to recover local stresses associated to local deformations with reasonable quality.

However, it must be said that this objective has not been achieved completely, only partially. It has been observed that the more complex the model, the worse the computational efficiency, and the advantages of performing an EMBS simulation against a finite-element simulation are much less significant. Also, in this thesis, with the more complex model, some parameters, such as the c_p and the β_R, are determined by trial and error, which reduces the efficiency of the whole process.

To assemble the EMBS models, four different model order reduction techniques have been used: Modal truncation, a Craig Bampton method, dynamic condensation and CMS-Gram methods. In short, it can be said that the modal truncation allows the researcher to integrate the problem in a very efficient manner but only the kinematics and the contact forces can be recovered.

The other three techniques are able to recover local deformations and stresses in an area in which a force is applied in a similar way. Comparing these three techniques, the matrices computed with the CMS-Gram algorithm provides the

best results in terms of accuracy with the three models tested (Beam, single gear and the gear pair). However, accuracy is achieved at the expense of a significantly greater pre-processing step, both in computational time and resources, to assemble the reduction matrix.

To conclude the work, attention should be drawn to two aspects in order to improve EMBS simulations in future jobs. During the development of this thesis it could not be explained in detail why a significant level of material damping is needed when the EMBS simulation is performed but not when the same simulation is done with the FE solver. It is known that the FE integration scheme somehow damps the system even though no damping has been explicitly defined. Nevertheless, since introducing significant levels of damping in the EMBS simulations entails an increase in the computational time, it would be interesting to research into different types of reduction matrices that minimize the problem.

In this sense, the deformation pattern of the gear obtained with the FE solver is fed back to assemble a reduction matrix in combination with eigenmodes. With this kind of matrix it is possible to image stresses better than with a modal truncation and still reduce the oscillations in comparison with other reduction techniques. However, the results obtained are not satisfactory and obviously, these kinds of matrices do not have practical utility.

Finally, more in-depth research needs to be done into the strength of the EMBS software, i.e. *GTM*, in the face of numerical problems and singularities, e.g. the squared section beam model. In this case, neither nodal deformation nor stresses could be recovered. It would be interesting to know if this is a particular case or if it is worth reinforcing the EMBS software against these kinds of numerical hitches.

Appendix

A.1 Content of the CD-ROM

The attached CD-ROM contains the following data structure:

- **DIPL-MSC_215.pdf**: pdf file of the master thesis DIPL-MSC–215.

- **DIPL-MSC_215/**:directory with the *.tex files of the report DIPL-MSC–215 composed with LaTeX as well as all the corresponding *.eps and *.svg figures.

- **DATA/**: a directory with all the relevant data used in this work

Additional information is found in the readme.txt files of the directories.

List of Figures

List of Tables

Bibliography

[Agullo00] Agullo, J.: Mecanica de la Particula y el Solido Rigido. Ok Punt Publicaciones, 2000.

[Balmes05] Balmes, E.: Modes and Regular Shapes. How to extend Component Mode Synthesis Theory. In Proceedings of the 11th DINAME, Ouro Preto, Brazil, February 28 - March 4. 2005.

[BednarekKowalczyk11] Bednarek, T.; Kowalczyk, P.: Improvement of Penalty Approach in Contact Modeling. In 19th International Conference on Computer Methods in Mechanics (CMM 2011), 9-12.05.2011, Warszawa, pp 127-8. 2011.

[CraigBampton68] Craig, R.; Bampton, M.: Coupling of Substructures for Dynamic Analyses. AIAA Journal, Bd. 6, Nr. 7, S. 1313–1319, 1968.

[Eberhard00] Eberhard, P.: Kontaktuntersuchungen durch hybride Mehrkörpersystem/ Finite Elemente Simulationen (in German). Shaker Verlag, 2000.

[FehrLehnerEberhard07] Fehr, J.; Lehner, M.; Eberhard, P.: On the Automated Generation of Reduced Order Models in Flexible Multibody Dynamics. In Proceedings in Applied Mathematics and Mechanics. 2007.

[GimenezJalon84] Gimenez, J.; de Jalon, J.G.: Teoria y Practica del Analisis Modal. Escuela Superior de Ingenieros Industriales de San Sebastian. Universidad de Navarra, 1984.

[Griffer10] Griffer, D.: Linear Algebra and its Applications- More Advanced (Paper) V2. Ellis Horwood Ltd, 2010.

[HolzwarthEberhard] Holzwarth, P.; Eberhard, P.: SVD-Based Improvements for Component Mode Synthesis in Elastic Multibody Systems. European Journal of Mechanics - A/Solids (submitted for publication, 2013).

[JalonBayo94] de Jalon, J.G.; Bayo, E.: Kinematic and Dynamic Simulation of Multibody Systems: The Real Time Challenge. Springer-Verlag, 1994.

[LehnerEberhard07] Lehner, M.; Eberhard, P.: A Two-Step Approach for Model Reduction in Flexible Multibody Dynamics. Multibody System Dynamics, Bd. 17, Nr. 2-3, S. 157–176, 2007.

[MeirovitchKwak90] Meirovitch, L.; Kwak, M.: Convergence of the Classical Rayleigh-Ritz Method and the Finite Element Method. AIAA Journal, Bd. 28, S. 1509–1516, 1990.

[Nour-OmidWriggers87] Nour-Omid, B.; Wriggers, P.: A Note on the Optimun Choice for Penaly Parameters. Comunication in Applied Numerical Methods, Bd. 3, S. 581–585, 1987.

[NowakowskiEtAl12] Nowakowski, C.; Fehr, J.; Fischer, M.; Eberhard, P.: Model Order Reduction in Elastic Multibody Systems using the Floating Frame of Reference Formulation. In Proceedings MATHMOD 2012 - 7th Vienna International Conference on Mathematical Modelling. Vienna, Austria, 2012.

[SchwertassekWallrappShabana99] Schwertassek, R.; Wallrapp, O.; Shabana, A.: Flexible Multibody Simulation and Choice of Shape Functions. Nonlinear Dynamics, Bd. 20, S. 361–380, 1999.

[SeifriedSchiehlenEberhard10] Seifried, R.; Schiehlen, W.; Eberhard, P.: The Role of the Coefficient of Restitution on Impact Problems in Multibody Dynamics. Proceedings of the Institution of Mechanical Engineers, Part K: Journal of Multi-body Dynamics, Bd. 224, Nr. 3, S. 279–306, 2010.

[Shabana98] Shabana, A.A.: Dynamics of Multibody Systems. Cambridge: Cambridge University Press, 1998.

[TobiasEberhard09] Tobias, C.; Eberhard, P.: A Method for Stress Recovery in Reduced Flexible Multibody Systems. In Proceedings Multibody Dynamics 2009 - ECCOMAS Thematic Conferences, Warsaw, Poland, 29 June - 2 July. Warsaw, Poland, 2009.

[Wilkinson63] Wilkinson, J.: Rounding Errors in Algebraic Problems. Prentice Hall, Englewood Clifffs, N.J., 1963.

[Ziegler12] Ziegler, P.: Dynamische Simulation von Zahnradkontakten mit elastischen Modellen (in German). Dissertation, Schriften aus dem Institut für Technische und Numerische Mechanik der Universität Stuttgart, Band 23. Aachen: Shaker Verlag, 2012.

Erklärung

Hiermit versichere ich, dass ich

- die vorliegende Arbeit selbständig verfasst habe,
- keine anderen als die angegebenen Quellen benutzt und alle wörtlich oder sinngemäß aus anderen Werken übernommenen Aussagen als solche gekennzeichnet habe,
- die eingereichte Arbeit weder vollständig noch in Teilen bereits veröffentlicht habe und
- dass das elektronische Exemplar mit den anderen Exemplaren übereinstimmt.

Datum	Unterschrift